The Astrophysical Journal, 934:173 (19pp), 2022 August 1 https://doi.org/10.3847/1538-4357/ac77fd

The ALMaQUEST Survey. VIII. What Causes the Discrepancy in the Velocity between the CO and Hα Rotation Curves in Galaxies?

Yung-Chau Su[1,2], Lihwai Lin[2], Hsi-An Pan[3], Carlos López Cobá[2], Bau-Ching Hsieh[2], Sebastián F. Sánchez[4], Mallory D. Thorp[5], Martin Bureau[6,7], and Sara L. Ellison[5]
[1] Department of Physics, National Taiwan University, No. 1, Section 4, Roosevelt Road, Taipei 10617, Taiwan
[2] Institute of Astronomy and Astrophysics, Academia Sinica, No. 1, Section 4, Roosevelt Road, Taipei 10617, Taiwan
[3] Department of Physics, Tamkang University, No.151, Yingzhuan Road, Tamsui District, New Taipei City 251301, Taiwan
[4] Instituto de Astronomía, Universidad Nacional Autónoma de México, Circuito Exterior, Ciudad Universitaria, Ciudad de México 04510, Mexico
[5] Department of Physics & Astronomy, University of Victoria, Finnerty Road, Victoria, British Columbia, V8P 1A1, Canada
[6] Sub-department of Astrophysics, University of Oxford, Denys Wilkinson Building, Keble Road, Oxford OX1 3RH, UK
[7] Yonsei Frontier Lab and Department of Astronomy, Yonsei University, 50 Yonsei-ro, Seodaemun-gu, Seoul 03722, Republic of Korea
Received 2021 May 30; revised 2022 May 24; accepted 2022 June 11; published 2022 August 4

Abstract

We compare the CO(1–0) and Hα kinematics in 34 nearby galaxies, selected from the ALMaQUEST and EDGE-CALIFA surveys. We use 3D-Barolo, a 3D tilted-ring model, to derive the CO and Hα rotation curves. Before comparing rotation curves in the 34 nearby galaxies, we found systematics between the MaNGA and CALIFA data using eight MaNGA-CALIFA overlapping galaxies. We assume the rotation curves based on the MaNGA data are accurate and made the corresponding correction to the CALIFA data. Our result shows that ∼56% (19/34) of our galaxies present slower Hα rotation curves compared to the CO rotation curves, with a median value of 6.5 km s^{-1}. The remaining galaxies (15/34) show consistent CO–Hα rotation velocity within uncertainties. As a result, the Hα rotation may underestimate the total dynamical mass by 6% for a circular velocity of 200 km s^{-1} (the median value in our sample). Furthermore, the difference in the velocity between the CO and Hα rotational velocity is found to correlate with the difference in velocity dispersion between CO and Hα, suggesting that gas pressure plays a role in the discrepancy in velocity. After incorporating the effect of pressure support due to the turbulent gas motion into our sample, the median value of the difference in the velocities decreases to 1.9 km s^{-1}, which in turn reduces the underestimation of the dynamical mass to ∼2%. Finally, we also investigate the role that the extraplanar diffuse ionized gas plays in the discrepancy in the velocity of CO–Hα.

Unified Astronomy Thesaurus concepts: Galaxy kinematics (602); Galaxy rotation (618); Interstellar medium (847); Galaxy dynamics (591); Molecular gas (1073); Optical astronomy (1776); Radio astronomy (1338)

1. Introduction

The galaxy rotation curve is the relation between the mean orbital speed of stars or gas in a given galaxy and the radial distance from the galactic center. Practically, the rotation curves in galaxies can be measured by the redshifted emission or absorption lines such as the H I 21 cm line (tracing the atomic gas), CO emission line (tracing the molecular gas), Hα line (tracing the ionized gas), and stellar absorption lines (tracing the stars), as described in detail in Sofue & Rubin (2001). One of the important applications of rotation curves is the constraint on the dynamical mass distribution, which provides strong evidence of the presence of dark matter (Sofue & Rubin 2001; de Blok et al. 2008). To derive the dynamical mass from rotation curves, one important assumption is that the rotating disk in the galaxy's radial equilibrium is balanced by the centrifugal force and gravitational force. In other words, it assumes that the rotation velocity we measure is an optimal tracer of the circular velocity $V_c = \sqrt{R\frac{\partial \Phi}{\partial R}}$. This assumption requires the emitting material to be dynamically cold so that we can ignore the pressure term in the virial theorem (Dalcanton & Stilp 2010; Iorio et al. 2017).

Several studies have shown that CO is a good tracer of circular velocity (Davis et al. 2013; Leung et al. 2018; Lang et al. 2020). However, it seems not to be the case for the Hα emission line. Davis et al. (2013) compared the CO and ionized rotation curves in 24 early-type galaxies from the ATLAS3D survey. They found that 80% of their sample show slower ionized gas rotational velocities. The other 20% showed consistent CO and ionized rotation within uncertainties. They attribute the discrepancy in the systematic velocity to the presence of the pressure support of the ionized gas. Similar studies have also been carried out for late-type galaxies. Levy et al. (2018) compared the CO and ionized rotation curves in 17 rotation-dominated late-type galaxies, selected from the EDGE-CALIFA survey (Sánchez et al. 2012; Bolatto et al. 2017). They also found that 75% of their sample showed slower Hα rotational velocity than the molecular gas, while the other 25% showed consistent CO and Hα rotations within errors. They attribute this to the presence of extraplanar diffuse ionized gas (eDIG). Since the rotational velocity of eDIG is slower than the ionized gas on the midplane (Bizyaev et al. 2017; Levy et al. 2019), the eDIG could reduce the observed mean rotational velocity, producing an systematic offset in the rotational velocity between CO and ionized gas. These studies suggest that the discrepancy in the velocity of CO–Hα is common in nearby galaxies regardless of morphology types.

Understanding the reason behind such a discrepancy in the velocity of CO–Hα is important because the generation of mass

models has conventionally been done based on Hα rotation curves (Broeils & Courteau 1997; Östlin et al. 1999; de Blok et al. 2001; Kuzio de Naray et al. 2008; Epinat et al. 2009; Douglass et al. 2019) given that it is relatively easier to obtain a larger sample with the measurement of Hα rotation compared to other tracers. The lower velocity in Hα rotation implies that these mass models are potentially biased to a lower value. Hence, a comprehensive understanding of the discrepancy in the velocity of CO–Hα is important to quantify the potential mass bias based on Hα rotations.

The ALMA-MaNGA QUEnching and STar Formation (ALMaQUEST; Lin et al. 2020) and EDGE-CALIFA (Sánchez et al. 2012; Bolatto et al. 2017) surveys, which combined the CO(1–0) observations and integral field unit (IFU) spectroscopy data for 46 and 126 nearby galaxies, respectively, provide us with a good opportunity to compare CO and Hα rotation curves in a considerable amount of samples and also in a wide radial extension. Besides the high spatial and spectral resolution of CO(1–0) and Hα emission lines provided by these data sets, the spatially matched resolution in CO(1–0) and Hα observations make it more ideal to compare the molecular and ionized gas rotation curves. In this study, with the selected 34 nearby galaxies from the combined ALMaQUEST and EDGE-CALIFA data set, we aim to further investigate the discrepancy in the velocity of CO–Hα with a larger sample size.

In Section 2, we describe the data used in this study. Sections 3 and 4 present the method and tools we use to measure the CO and Hα rotation curves. The main results of this study and the interpretations of the discrepancy in the velocity of CO–Hα are given in Sections 5 and 6, respectively. Finally, we present the summary of this study in Section 7.

Throughout this paper, we adopt the following cosmology: $H_0 = 70\,\mathrm{km\,s^{-1}\,Mpc^{-1}}$, $\Omega_m = 0.3$, and $\Omega_\Lambda = 0.7$.

2. Data

2.1. MaNGA Survey

Mapping Nearby Galaxies at APO (MaNGA; Bundy et al. 2015) is an integral field unit (IFU) survey, which is part of SDSS-IV. With the technique of integral field spectroscopy, MaNGA provides the two-dimensional spatially resolved spectra of 10,000 galaxies in the range of $0.01 < z < 0.15$. The spectral coverage of MaNGA ranges from 3600–10,300 Å with spectral resolution $R \sim 2000$, which corresponds to $\sigma_{\rm inst} \approx 70\,\mathrm{km\,s^{-1}}$ at the wavelength of Hα. The spatial resolution of MaNGA is 2.″5, corresponding to the physical scale of 1.5 kpc at the average redshift (range from 1.1–5.9 kpc for the MaNGA sample included in this study). The spaxel size in the data products is 0.″5. Details about the MaNGA survey can be found in Bundy et al. (2015). The Hα data cubes for MaNGA galaxies are based on the SDSS Data Release 15 (DR15) analyzed through the MaNGA reduction pipeline (Law et al. 2016). The Hα data cubes used to measure the Hα rotation curves for MaNGA galaxies are taken from the MaNGA Data Analysis Pipeline (Westfall et al. 2019). The emission lines are extracted after subtracting the best-fit stellar continuum from the observed spectra. We only include the spaxels with a signal-to-noise ratio $(\mathrm{S/N}) > 3$ for the Hα flux in this study. The global star formation rate (SFR), stellar mass, and the Σ_* of the MaNGA galaxies used in this work are taken from the PIPE3D (Sánchez et al. 2016a, 2016b) value-added catalog (Sánchez et al. 2018).

2.2. CALIFA Survey

The Calar Alto Legacy Integral Field Area (CALIFA) survey contains spatially resolved spectroscopy for 667 nearby galaxies ($0.005 < z < 0.03$) (Sánchez et al. 2012, 2016c). CALIFA used PPAK IFU (Kelz et al. 2006) on board the Calar Alto 3.5 m telescope. The whole spectral coverage ranges from 3400 to 7300 Å, which is covered by two spectral gratings. The lower spectral resolution grating (V500) covers the range of 3745–7300 Å with spectral resolution $R \sim 850$, corresponding to $\sigma_{\rm inst} \approx 116\,\mathrm{km\,s^{-1}}$ at the Hα emission line. The high-resolution grating (V1200) covers the range of 3400–4750 Å with spectral resolution $R \sim 1650$, i.e., $\sigma_{\rm inst} \approx 75\,\mathrm{km\,s^{-1}}$. The typical spatial resolution of CALIFA is 2.″5, which corresponds to ∼0.8 kpc at the averaged redshift. More details about the selection procedure and statistical properties of galaxies in the CALIFA survey can be found in Walcher et al. (2014). The Hα data cubes for the CALIFA galaxies are taken from the PIPE3D Data products (Sánchez et al. 2016a, 2016b). Similar to the processing of the MaNGA Hα data, The Hα emission lines are extracted after subtracting the best-fit stellar continuum from the observed spectra (Sánchez et al. 2016a, 2016b), and only the spaxels with $\mathrm{S/N} > 3$ for Hα flux are included in this study.

2.3. EDGE Survey

The Extragalactic Database for Galaxy Evolution (EDGE) survey (Bolatto et al. 2017) comprises ^{12}CO($J = 1-0$; 115.2712 GHz) measurements for 126 nearby galaxies with CARMA in the D and E configurations. The parent sample of EDGE-CALIFA galaxies is observed in E configurations, which consists of 177 galaxies selected based on their infrared brightness and biased to the higher SFR in the CALIFA sample. The 126 galaxies are then selected and resampled in the D configuration and constitute the final EDGE-CALIFA data. More details about the EDGE-CALIFA survey can be found in Bolatto et al. (2017). The spatial resolution of the EDGE data is ∼4.″5, corresponding to the physical scale between 0.6 and 2.4 kpc for the EDGE sample included in this study. Since CALIFA and EDGE have different spatial resolutions, with EDGE having the worst resolution, we convolved the CALIFA data to match the EDGE resolution. We note that, in this case, the typical spatial resolution is similar to the spatial resolution of the MaNGA data. The spectral resolution is $\sigma_{\rm inst} \approx 20\,\mathrm{km\,s^{-1}}$ in the data cube. We use the *dilated* mask to exclude noise (Section 3.1.1 in Bolatto et al. 2017). The mask is created by starting at 3.5σ (or greater) peaks in at least two consecutive channel maps in the data cube and then it expands down to the surrounding 2σ contours. Finally, an additional pixel is added to capture the low-level emission. To investigate the discrepancy in the velocity of CO–Hα with a larger sample size, we include the sample used in Levy et al. (2018), which contains 17 star-forming, late-type galaxies. This set of galaxies is referred to as the EDGE-CALIFA Kinematic SubSample (EDGE-CALIFA KSS hereafter).

2.4. ALMaQUEST Survey

The ALMaQUEST survey contains ^{12}CO($J = 1-0$; 115.2712 GHz) MaNGA follow-up observation for 46 galaxies

with ALMA in the C43-2 configuration. The field of view for each galaxy is $\sim 50''$ with a spatial resolution of $\sim 2\farcs5$, which matches the MaNGA resolution. The spectral resolution of ^{12}CO(1−0) for ALMaQUEST galaxies is $\sigma_{\rm inst} \approx 11\,{\rm km\,s^{-1}}$. To investigate how gas drives the location and evolution of galaxies in the star-forming main sequence, the ALMaQUEST survey covers a broad range of specific SFRs, spanning from the green valley, main sequence, to the starburst regimes. More details on the ALMaQUEST survey can be found in Lin et al. (2020). In this study, we only include spaxels with S/N > 3 for ^{12}CO(1−0).

3. Method

In this section, we introduce the general methodology for both ALMaQUEST KSS and EDGE-CALIFA KSS.

3.1. Tilted-ring Model

The tilted-ring model (Rogstad et al. 1974; van Albada et al. 1985; Begeman 1989) is a technique widely used to describe the kinematics of spiral galaxies. The main assumptions of this technique are the following: (i) the emitting material is settled in a thin disk, (ii) the velocity of the rotation of the material only depends on the distance from the center, and (iii) the motion of the material is dominated by circular motion. Under these assumptions, the tilted-ring model breaks the rotating disk into a series of independent concentric rings with different radii, each of which has geometric and kinematic parameters. Since the rotating disk is not necessarily face-on from the line of sight, the projection of each ring on the sky is usually parameterized as an elliptical ring. For a given projected ring, the projected velocity along the line of sight $V_{\rm los}$ is given by

$$V_{\rm los} = V_{\rm sys} + V_{\rm rot}(R)\cos(\theta)\sin(i), \quad (1)$$

where $V_{\rm sys}$ is the systematic velocity of the galaxies, $V_{\rm rot}(R)$ is the deprojected rotational velocity of the ring with deprojected radius R, θ is the deprojected position angle (0° is at the major axis of the projected elliptical rings), and i is the inclination between the line of sight and the rotating disk (0° is face-on). The standard approach to applying the tilted-ring model is to fit 2D-velocity maps, but some drawbacks of such a 2D-fitting algorithm exist. The most severe one is the beam smearing effect, which tends to flatten the gradient of the velocity field (van den Bosch et al. 2000; Swaters et al. 2009). In this work, we adopt an alternative approach by using a 3D-fitting software based on the concept of the tilted-ring model called 3D-BAROLO (3DB hereafter; Di Teodoro & Fraternali 2015) to measure the kinematic and geometric parameters.

3.2. 3DB

3DB (Di Teodoro & Fraternali 2015) adopts a 3D tilted-ring model that fits the 3D data cube (two axes define sky coordinate and one axis defines spectrum direction) directly. In practice, 3DB fits the data cube ring by ring by building an artificial 3D model cube and finds the best fit by minimizing the residual calculated pixel by pixel between the data cube and the model cube. Before comparing the data cube and the model cube, the former needs to be convolved to the same spatial and spectral resolution as the latter. This ensures the full control of instrumental effects, such as the beam smearing effect, which can significantly influence the fitting result in the region where the velocity gradient is large.

The residual function to be minimized in this study can be expressed as

$$F = \frac{1}{n}\sum_{i=1}^{n} \Delta r_i w(\theta_i), \quad (2)$$

where n is the number of pixels, Δr is the residual at each pixel, $w(\theta)$ is the weighting function of the azimuthal angle. Δr and the weighting function can be expressed as

$$\Delta r = |M - D| \quad (3)$$

and

$$w(\theta) = |\cos(\theta)|^2, \quad (4)$$

where M and D are the flux values of the model and the data, respectively. θ is the position angle ($\theta = 0°$ for the major axis). We note that there is no intensity weighting in the residual function. Hence, the faint pixels carry the same weights as the bright ones.

In 3DB, each ring with deprojected radius R and width W is characterized by eight parameters: spatial coordinate of the center (x_0, y_0), $V_{\rm sys}$, $V_{\rm rot}$, velocity dispersion (σ_v), i, PA (the position angle between the north and the major axes, represented in degrees from the north in the counterclockwise direction), gas component surface density (Σ), and ring thickness along the axisymmetric axis (z_d).

In this work, we focus on the kinematic parameters $V_{\rm rot}$ and σ_v. To reduce the parameter space, some assumptions are made on other parameters before performing the fitting. First, we exclude the gas surface density from the fit by normalizing the flux in the model cube to that in the original data cube. Two different kinds of normalization are provided in 3DB: pixel by pixel and azimuthally averaged. In the former case, the integrated flux of each pixel in the model cube is normalized to that in the data cube. In the second case, the model is normalized to the azimuthal-averaged flux in each ring. More details can be found in Di Teodoro & Fraternali (2015). In this study, we apply the pixel-by-pixel approach since it allows us to account for the non-axisymmetric gas distribution. On the other hand, we fix the disk scale height to 100 pc. In Section 6.2, we discuss the impact of this assumption. Finally, we assume a constant inclination, position angle, systematic velocity, and kinematic center for each galaxy.

4. Analysis

4.1. Fit Rotation Curves

To derive reliable rotation curves from the tilted-ring model, it is crucial to set the initial parameters properly. The initial dynamical center is the photometric center and the initial values for inclinations and PAs are derived from the photometric fit from the NASA-Sloan Atlas (NSA) catalog (Blanton et al. 2011). The initial $V_{\rm sys}$ is calculated as the midpoint between the velocities corresponding to the 20% of the peaks of the global line profile (Di Teodoro & Fraternali 2015). We assume that all rings in each galaxy share the same dynamical center, inclination, position angle, and $V_{\rm sys}$. The initial values of rotational velocity and velocity dispersion are set to 100 and $30\,{\rm km\,s^{-1}}$, respectively.

We apply a two-step process to fit the rotation curves. In the first step, we use one unit of spatial resolution as the annulus

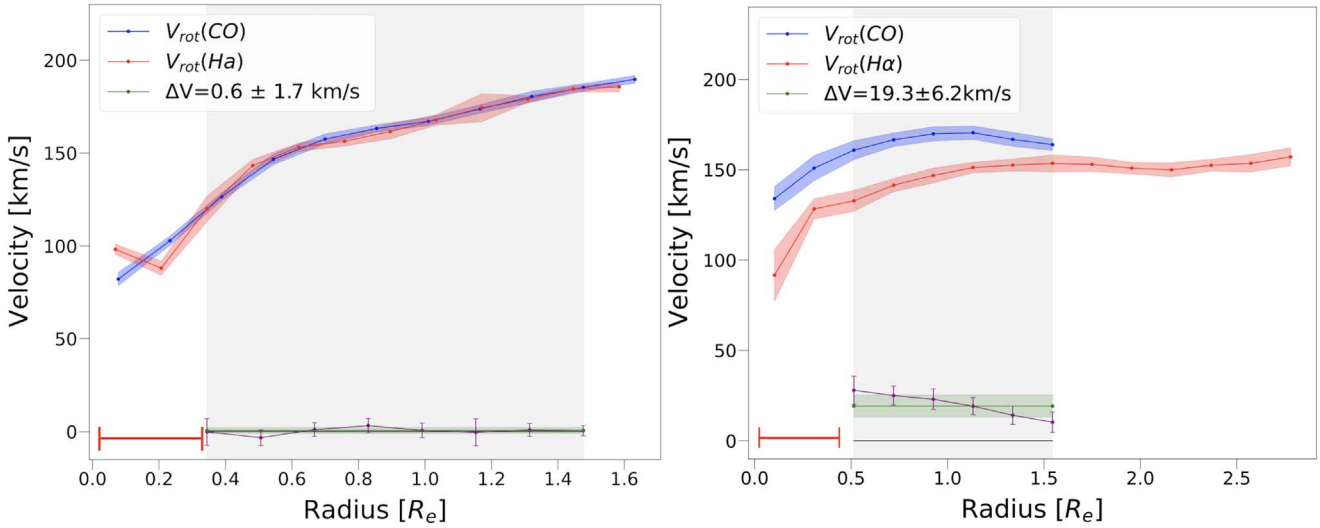

Figure 1. The left panel shows the rotation curves of one of our galaxies from the ALMaQUEST survey, 7815-12705. The blue one stands for $V_{\rm rot}$(CO) and the red one is $V_{\rm rot}$(Hα). ΔV, the variance weighted mean of the rotation difference between $V_{\rm rot}$(CO) and $V_{\rm rot}$(Hα), is calculated within the gray area and is presented as the green line. The purple line shows the differences in the velocity in each radius. The error of ΔV is the standard deviation of the differences in the velocity in sample points. The shadow areas present the errors of each quantity. The red bar at the lower-left corner shows the beam size. The right panel shows the rotation curves in NGC 5520, one of the galaxies in the EDGE-CALIFA survey that shows the discrepancy in the velocity of CO–Hα. We note that, in general, the radial range where we compare the CO and Hα rotation curves is similar between the ALMaQUEST samples and the EDGE-CALIFA samples, which covers $\sim$0.3 to $\sim$1.5R_e.

width and fit the geometric parameters, rotation curves, and velocity dispersion at the same time. The purpose of the first step is to obtain reliable geometric parameters. In the second step, we fix the geometric parameters and fit the rotational velocity and velocity dispersion with half of the unit of the spatial resolution as the annulus width. These two steps ensure an accurate rotation curve measurement.

In the new version, we quantify the errors by 3DB's method for both the rotational velocity and velocity dispersion. After finding the best model by minimizing the residual function, 3DB normalizes the value of the minimum of the residual function. Then, 3DB calculates a number of models by a Gaussian distribution oversampling. The center of the Gaussian distribution is the point that minimizes the residual function in the parameter space. Errors for each parameter are determined by the range where the residual increases 5% with respect to the minimum, i.e., the range where the residual function is smaller than 1.05. More details can be found in Di Teodoro & Fraternali (2015).

When measuring the rotation curves in galaxies, one of the important issues is the beam smearing effect, which causes the degeneracy between rotational velocity and velocity dispersion, and flattens the velocity gradient (e.g., van den Bosch et al. 2000; Swaters et al. 2009). The beam smearing effect becomes significant in the case where the velocity gradient is large, which is usually in the central region of a galaxy. Although 3DB allows better control of such an instrumental effect compared to the 2D-fitting methods, some issues were found when measuring the central rotation curves, which will be discussed in more detail in Section 5.1. The Hα rotation curves for our sample are fit using the same method under the assumption that CO and Hα are coplanar. In other words, CO and Hα share the same kinematic center, inclination, and position angle.

4.2. Subsample Selected for This Study

To reliably measure rotation curves by the tilted-ring model, there are practical upper and lower limits on the inclination of galaxies, as discussed in de Blok et al. (2008). For high-inclination galaxies, it is difficult to derive rotation curves since the line of sight penetrates several layers at different distances from the center. For low-inclination galaxies, the decreased projected component of the rotational velocity makes it difficult to derive reliable rotation curves. As adopted by de Blok et al. (2008), the practical upper and lower limits of inclination are suggested to be 40° and 75°, respectively. We further exclude galaxies that show apparent bar structures, interacting galaxies, and galaxies with distorted morphology through visual inspection, as similarly done by Aquino-Ortíz et al. (2020). This selection makes sure that the gas motion is dominated by rotation and also validates the assumption of constant inclination and position angle. After applying these selection criteria to the ALMaQUEST galaxies, 17 galaxies are selected and referred to as the ALMaQUEST Kinematic SubSample (ALMaQUEST KSS hereafter). We note that the 17 galaxies from the EDGE-CALIFA KSS fit well with these selection criteria. The result of this research is based on the study of the combined 17 ALMaQUEST KSS and the 17 galaxies from EDGE-CALIFA KSS.

5. Result

5.1. Systematic Discrepancy between the CO and Hα Rotation

Previous studies in the literature have found that Hα tends to rotate either consistently or slower than CO (Simon et al. 2005; Davis et al. 2013; Levy et al. 2018). In this study, we show that the discrepancy in the velocity of CO–Hα is seen in both ALMaQUEST KSS and EDGE-CALIFA KSS. The left panel in Figure 1 shows an example selected from the ALMaQUEST survey with consistent CO and Hα rotation. As a comparison, the right panel shows a galaxy from the EDGE-CALIFA survey, which has an apparent discrepancy in the velocity between CO and Hα rotation. The same plots for all the galaxies included in this study can be found in Figures C1 and C2. We note that, although the galaxies in the CALIFA survey are covered up to a 2.5 effective radius (R_e; Walcher et al. 2014), which is

larger than that of MaNGA galaxies ($1.5R_e$; Bundy et al. 2015), the radial range in which we compare the CO and Hα rotation curves are set to be between 0.3 and $1.5R_e$ for both the ALMaQUEST and EDGE-CALIFA samples that are constrained by the coverage of CO. On the other hand, as we can see, there is a turnover feature shown in Hα rotation curves in the central region. Such a feature is commonly found in the Hα rotation curves among our samples. To test if this feature is artificial, we degrade the spectral resolution of our CO data cubes, which have an original spectral resolution $\sigma_{\rm inst} \approx 11\,{\rm km\,s^{-1}}$, to the spectral resolution of MaNGA Hα data ($\sigma_{\rm inst} \approx 70\,{\rm km\,s^{-1}}$) by convolving them with a Gaussian kernel along the spectral axis. After fitting the convolved data using 3DB, we found such a feature also appears in the CO rotation curves. This phenomenon might be caused by the following two effects: (i) it is more difficult to derive reliable rotational velocity and velocity dispersion at the same time with a low spectral resolution; (ii) there are fewer data points in the most central region, which make it difficult to construct a reliable fit result. In this study, we exclude the fit result of the rotation curves within one resolution area from the center in the following analysis.

To quantify the difference in the velocity between the CO and Hα rotation curves for a given galaxy, we first linearly interpolate the Hα rotation curve and resample the Hα rotational velocity at the same radii where we sample the CO rotational velocity. Then, for each galaxy, we calculate the difference in the velocity between CO and Hα rotation at each radius. We define ΔV for an individual galaxy as the variance weighted mean of the differences in velocity $V_{\rm rot,CO} - V_{\rm rot,H\alpha}$. $\sigma_{\Delta V}$, the error of ΔV, is defined as the standard deviation of the differences in velocity. In this study, we say that a galaxy has a discrepancy in the velocity of CO–Hα if $\Delta V > \sigma_{\Delta V}$ and has consistent CO–Hα rotation if $\Delta V \leqslant \sigma_{\Delta V}$.

As the spectral resolution differs between the MaNGA and CALIFA data cubes, it is important to quantify whether there exists systematics or not in the measurement of the Hα rotation curves due to the difference in the instrumental characteristics. To conduct this test, we select in total eight galaxies that are included in the main samples of both the MaNGA and CALIFA surveys.[8] When comparing the rotation curves of the eight MaNGA-CALIFA overlapping galaxies, we found systematics between the rotation curves fitted from the MaNGA Hα data cubes and that fitted from the CALIFA Hα data cubes. The latter tend to have slower rotational velocity. We adopt the definition of ΔV and use it to quantify the differences in velocity between the MaNGA Hα and the CALIFA Hα rotation curves in these eight overlapping galaxies (labeled as $\Delta V_{\rm MC}$). The median value of $\Delta V_{\rm MC}$ in these eight galaxies is $9.8\,{\rm km\,s^{-1}}$. Finally, we use a bootstrap method to test if this systematic is reliable, and a median value of $\Delta V = 8.5$ with a standard deviation of $1.3\,{\rm km\,s^{-1}}$ is found. In Appendix B, we discuss the details of this test. This systematics causes ΔV in the EDGE-CALIFA KSS to become larger (or smaller in ALMaQUEST KSS). To compensate for this systematics, we subtracted ΔV in CALIFA KSS by $8.5\,{\rm km\,s^{-1}}$. All discussions hereafter include this correction.

On the other hand, given the fact that the physical spatial resolutions of ALMaQUEST KSS and EDGE-CALIFA KSS are similar to each other, it is unlikely that the spatial resolution would raise an issue about the systematics between these two data sets. Figure 2 shows the relation between ΔV and the physical spatial resolutions. As we can see, the physical spatial resolutions of the two data sets are comparable. Moreover, the lack of trend between ΔV and the physical spatial resolutions is also found. The same results are found for the case which does not apply the MaNGA-CALIFA systematics correction to the EDGE-CALIFA KSS.

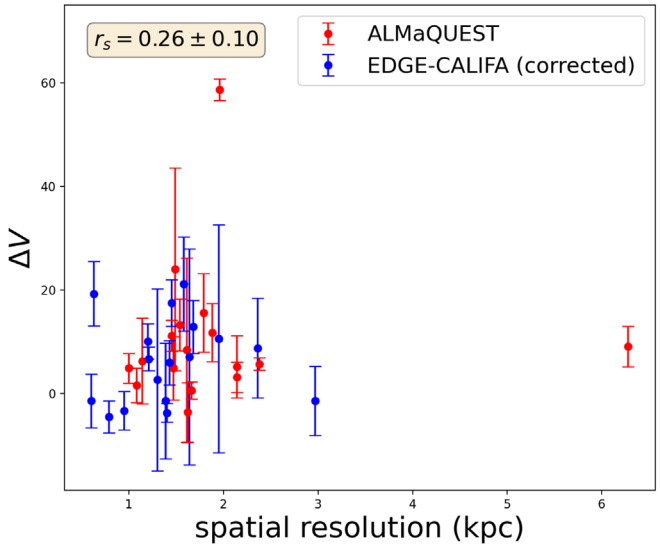

Figure 2. The relation between ΔV and the physical spatial resolution for ALMaQUEST KSS (red points) and EDGE-CALIFA (blue points).

Based on the definition of ΔV, ~56% (19/34) of the sample shows a higher CO rotational velocity, while ~44% (15/34) of the sample shows consistent CO–Hα rotation. Some important parameters from the result of the 3DB fit are listed in Tables 1 and 2.

Figure 3 shows the normalized ΔV kernel density distribution (KDD) of our galaxies. In this figure, we use a normalized Gaussian kernel to represent a galaxy that is centered at ΔV with the dispersion $\sigma_{\Delta V}$. After summing all the Gaussians, the total distribution histogram is normalized to the unit area again. As we can see, the KDD shows that CO tends to have a higher rotation speed. The median ΔV of the ALMaQUEST+EDGE-CALIFA KSS galaxies is $6.5\,{\rm km\,s^{-1}}$. In general, The distribution of ΔV in EDGE-CALIFA KSS (after correcting for the MaNGA-CALIFA systematics described in Appendix B) is similar in comparison to ALMaQUEST KSS.

Figure 4 shows the relation between ΔV and the radial mean of $\sqrt{\sigma^2_{\rm H\alpha} - \sigma^2_{\rm CO}}$ for each individual galaxy. The differences in velocity dispersion are calculated within the region where ΔV is calculated. As we can see, there is a positive trend between these two parameters. We run a Spearman correlation analysis and find that the correlation coefficients give $r_s = 0.51 \pm 0.19$, 0.86 ± 0.22, and 0.71 ± 0.14 for ALMaQUEST KSS, EDGE-CALIFA KSS, and the combined sample, respectively. Since the magnitude of the velocity dispersion is related to the magnitude of the pressure gradient in the radial direction (Dalcanton & Stilp 2010; Davis et al. 2013; Levy et al. 2018), this gives us a hint that the radial pressure support may be responsible for the discrepancy in the velocity of CO–Hα. We will discuss this scenario in Section 5.2.

We also study the dependence of ΔV on other global parameters, such as the SFR, stellar mass (M_*), and specific

[8] These eight galaxies are independently selected and are not part of the ALMaQUEST nor the EDGE-CALIFA samples.

Table 1
Parameters of ALMaQUEST KSS

Name	z[a]	Sérsic Index[a]	$\log_{10}(M_*)$[b] ($M_\odot$)	$\log_{10}$(SFR)[b] ($M_\odot \mathrm{yr}^{-1}$)	log(sSFR)[b] (yr^{-1})	Inc[c] (°)	PA[c] (°)	CO $V_{\max}$ (km s^{-1})	ΔV (km s^{-1})	σ_{CO}[d] (km s^{-1})	$\sigma_{\mathrm{H}\alpha}$[e] (km s^{-1})
7815-12705	0.0293	1.1	10.77	0.8	−10.0	67	319	189.7 ± 2.0	0.6 ± 1.7	14.9 ± 1.0	35.7 ± 5.4
7977-3704	0.027	3.2	10.45	−0.59	−11.0	48	221	193.0 ± 1.5	11.2 ± 3.0	1.2 ± 1.5	31.8 ± 8.8
7977-12705	0.0269	4.8	11.02	0.66	−10.4	50	210	276.7 ± 5.5	24.0 ± 19.6	16.2 ± 2.5	64.2 ± 6.8
8077-9101	0.0429	2.2	10.42	−0.08	−10.5	76	51	190.9 ± 0.9	5.2 ± 6.0	9.8 ± 1.3	39.0 ± 6.8
8078-6103	0.0282	1.9	10.8	0.51	−10.3	51	165	215.6 ± 2.8	-3.6 ± 5.7	15.7 ± 1.3	32.2 ± 6.7
8078-12701	0.0267	3.5	11.12	0.37	−10.8	65	195	256.5 ± 3.8	8.4 ± 17.8	18.1 ± 0.8	32.7 ± 4.4
8081-9101	0.0282	1.8	10.73	0.41	−10.3	71	289	214.5 ± 4.1	4.9 ± 6.1	17.3 ± 1.1	45.2 ± 6.2
8081-9102	0.0336	2.0	10.81	0.17	−10.6	74	100	239.8 ± 3.7	15.6 ± 7.6	17.9 ± 1.1	44.5 ± 5.7
8082-12701	0.0268	2.9	10.53	0.07	−10.5	51	9	179.0 ± 1.4	4.9 ± 2.9	2.4 ± 0.8	36.8 ± 4.4
8082-12704	0.1317	5.3	11.66	−0.31	−12.0	62	163	322.2 ± 5.0	9.1 ± 3.9	15.2 ± 1.9	45.9 ± 8.8
8084-12705	0.0252	1.9	10.6	−0.06	−10.7	74	62	181.9 ± 2.3	13.3 ± 5.0	11.4 ± 1.2	35.1 ± 6.2
8086-9101	0.0398	6.0	11.12	−0.09	−11.2	63	265	256.1 ± 1.0	3.2 ± 2.9	3.4 ± 1.1	39.0 ± 5.7
8615-9101	0.0332	2.0	10.78	0.01	−10.8	74	351	218.5 ± 3.2	11.8 ± 5.6	13.9 ± 1.2	36.6 ± 6.1
8615-12702	0.0207	1.2	10.21	0.1	−10.1	75	318	102.0 ± 1.4	1.6 ± 3.3	8.2 ± 1.1	28.1 ± 5.7
8618-9102	0.0431	0.7	10.47	0.42	−10.0	73	327	159.5 ± 3.1	5.7 ± 1.2	6.3 ± 1.9	31.8 ± 7.6
8655-12705	0.0452	2.4	10.51	−1.55	−12.1	58	199	205.3 ± 2.7	58.7 ± 2.1	5.3 ± 1.8	48.0 ± 8.9
8952-12701	0.0282	1.6	10.78	−0.66	−11.4	58	27	218.9 ± 2.2	6.3 ± 8.3	0.7 ± 1.5	29.3 ± 5.8

Notes.
[a] From the SDSS NSA catalog.
[b] From Lin et al. (2020).
[c] 3DB fit result.
[d] The radial averaged velocity dispersion derived from the 3DB fit result. The region within one beam from the center is excluded from the calculation. For 8952-12701, which is a lack of CO detection in the central region, we start the sampling from four beams away from the center.
[e] The radial averaged velocity dispersion derived from the 3DB fit result. The region within one beam from the center is excluded from the calculation.

Table 2
Parameters of EDGE-CALIFA KSS

Name	z[a]	Sérsic Index[a]	$\log_{10}(M_*)$[b] ($M_\odot$)	$\log_{10}$(SFR)[b] ($M_\odot yr^{-1}$)	log(sSFR)[b] (yr^{-1})	Inc[c] (°)	PA[c] (°)	CO $V_{\max}$ (km s^{-1})	ΔV (km s^{-1})	σ_{CO}[d] (km s^{-1})	$\sigma_{\mathrm{H}\alpha}$[e] (km s^{-1})
IC 1199	0.0164	0.8	10.78	0.1	−10.7	69	160	198.6 ± 3.5	7.1 ± 20.8	5.4 ± 2.1	32.5 ± 7.9
NGC 2253	0.012	1.6	10.81	0.11	−10.7	41	120	190.0 ± 9.2	-1.4 ± 11.2	3.6 ± 2.0	28.3 ± 8.1
NGC 2347	0.0146	2.3	11.04	0.1	−10.9	50	9	287.3 ± 4.5	15.5 ± 4.5	5.5 ± 2.2	44.2 ± 8.7
NGC 2410	0.0157	2.9	11.03	0.1	−10.9	72	37	253.2 ± 5.8	21.2 ± 9.1	5.9 ± 1.9	49.9 ± 6.6
NGC 3815	0.0126	1.6	10.53	0.09	−10.4	64	245	191.6 ± 5.8	10.1 ± 3.4	6.6 ± 2.2	34.6 ± 8.8
NGC 4047	0.0114	1.5	10.87	0.1	−10.8	41	286	219.2 ± 2.8	6.7 ± 2.3	5.0 ± 2.2	26.7 ± 8.7
NGC 4644	0.0165	1.5	10.68	0.11	−10.6	66	237	188.4 ± 6.3	12.9 ± 5.1	6.2 ± 2.2	38.6 ± 8.8
NGC 4711	0.0136	0.9	10.58	0.09	−10.5	64	40	161.9 ± 2.3	-3.7 ± 1.8	2.8 ± 1.8	26.0 ± 7.0
NGC 5016	0.0087	1.3	10.47	0.09	−10.4	43	239	177.2 ± 6.0	-3.3 ± 3.7	5.2 ± 2.0	22.7 ± 8.0
NGC 5480	0.0065	1.0	10.18	0.08	−10.1	45	3	124.1 ± 5.8	-1.4 ± 5.2	3.8 ± 1.5	30.3 ± 6.2
NGC 5520	0.0062	3.2	10.07	0.11	−10.0	53	65	170.4 ± 3.7	19.3 ± 6.2	5.2 ± 2.1	35.1 ± 8.0
NGC 5633	0.0079	0.8	10.4	0.11	−10.3	48	197	176.8 ± 5.0	-4.5 ± 3.1	6.7 ± 1.8	25.5 ± 7.5
NGC 5980	0.0137	1.3	10.81	0.1	−10.7	69	195	221.9 ± 4.5	2.7 ± 17.6	8.1 ± 2.1	35.3 ± 6.2
UGC 04132	0.0174	0.8	10.94	0.12	−10.8	68	29	257.6 ± 5.7	10.6 ± 22.0	14.1 ± 1.9	47.0 ± 6.5
UGC 05111	0.0224	2.0	10.82	0.12	−10.7	73	300	232.3 ± 4.1	8.8 ± 9.6	10.7 ± 1.8	41.0 ± 6.5
UGC 09067	0.0263	1.5	10.96	0.12	−10.8	64	194	216.0 ± 7.6	-1.4 ± 6.7	5.6 ± 2.2	28.1 ± 8.6
UGC 10384	0.0167	1.3	10.33	0.14	−10.2	73	91	185.1 ± 5.8	6 ± 4.3	16.4 ± 1.9	37.8 ± 8.0

Notes.
[a] From the SDSS NSA catalog.
[b] From Bolatto et al. (2017).
[c] 3DB fit result.
[d] The radial averaged velocity dispersion derived from the 3DB fit result. The region within one beam from the center is excluded from the calculation.
[e] The radial averaged velocity dispersion derived from the 3DB fit result. The region within one beam from the center is excluded from the calculation.

star formation rate (sSFR), morphology, inclination, CO $V_{\max}$, as well as on the Σ_{SFR} and Σ_{M_*} within the area where ΔV is calculated. These plots are shown in Figure C3. Except for the Sérsic index, we did not find any apparent trend between ΔV and other parameters. These plots suggest that (i) no correlation was found between ΔV and the inclination; (ii) ΔV tends to be smaller in late-type galaxies (our galaxies are biased toward the late-type, though).

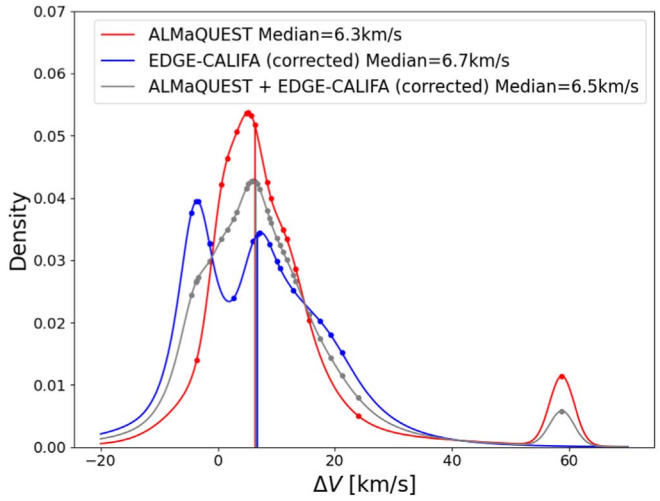

Figure 3. KDD of ΔV. Each galaxy is presented as a normalized Gaussian kernel with dispersion $\sigma_{\Delta V}$ and centered at ΔV. The gray curve shows the ΔV KDD in our whole sample. The red curve shows the KDD for ALMaQUEST KSS. The blue curve shows the KDD for EDGE-CALIFA KSS after correcting for the MaNGA-CALIFA systematics.

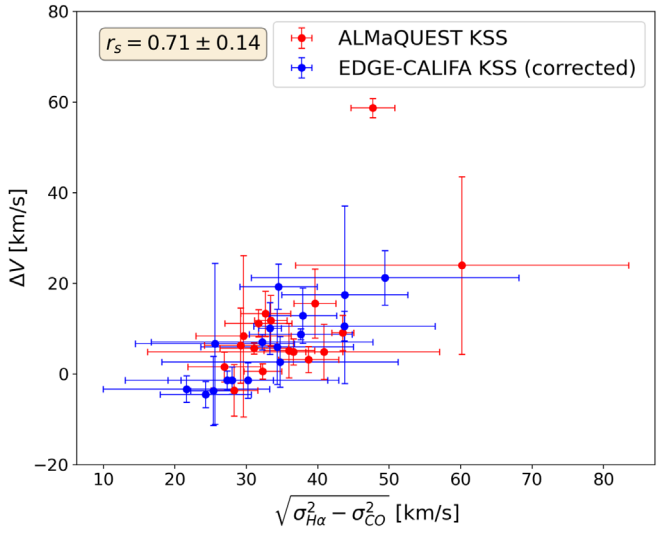

Figure 4. The difference in the rotational velocity between CO and Hα (ΔV) vs. the radial mean of $\sqrt{\sigma^2_{\rm H\alpha} - \sigma^2_{\rm CO}}$ for the ALMaQUEST KSS (red points) and EDGE-CALIFA KSS (blue) samples. The error of the difference in the velocity dispersion is characterized by the standard deviation of the measurements in the annuli. The Spearman correlation coefficient (r_s) shown in the upper-left corner is for the combined sample, which yields a strong correlation. The r_s for ALMaQUEST KSS and EDGE-CALIFA KSS are 0.51 ± 0.19 and 0.86 ± 0.22, respectively. The positive correlation between ΔV and the velocity dispersion quadrature suggests that the gas pressure contributes to the discrepancy in the velocity of CO–Hα.

5.2. Radial Pressure Support

Under the condition that gas motion is in equilibrium, the relation between the gravitational potential (Φ) and $V_{\rm rot}$ can be expressed by the following equation (Iorio et al. 2017):

$$\frac{1}{\rho}\frac{\partial P}{\partial R} = -\frac{\partial \Phi}{\partial R} + \frac{V^2_{\rm rot}}{R}, \tag{5}$$

where ρ is the volumetric density of the gas, and P is the gas pressure. Under the assumption that turbulence pressure dominates the pressure term, the pressure term can be expressed as $\rho\sigma_v^2$ (Dalcanton & Stilp 2010), where σ_v is the velocity dispersion. From Equation (5), we can find that $V_{\rm rot}$ is not a direct tracer of Φ if the pressure term is non-negligible. The asymmetric drift V_A is defined as

$$V_A^2 = V_c^2 - V^2_{\rm rot} = -\frac{R}{\rho}\frac{\partial \rho\sigma_v^2}{\partial R}, \tag{6}$$

where $V_c = \sqrt{R\frac{\partial \Phi}{\partial R}}$ is the circular speed. This could explain the discrepancy in the velocity of CO–Hα if the V_A term for the Hα source is large. That is, there is larger radial pressure supporting the ionized gas that produces Hα emission. Under the assumption of a thin disk and isotropic velocity dispersion, V_A can be expressed as

$$V_A^2 = -R\sigma_v^2\frac{\partial ln(\sigma_v^2 \Sigma_{\rm obs}\cos i)}{\partial R}. \tag{7}$$

Since 3DB can fit $V_{\rm rot}$, σ_v, and gas surface density simultaneously, we can calculate the V_A for CO and Hα and determine the intrinsic circular velocity. Such a process is called asymmetric drift correction (ADC hereafter; Iorio et al. 2017). If this scenario can fully explain the *discrepancy in the CO–Hα velocity*, we should expect

$$\sqrt{V^2_{\rm rot,CO} + V^2_{A,\rm CO}} \approx \sqrt{V^2_{\rm rot,H\alpha} + V^2_{A,\rm H\alpha}}. \tag{8}$$

5.2.1. Notes on the ADC

From Equations (6) and (7), one needs to assume a constant scale height and exponential distribution in the vertical direction, which is adopted in this study. A detailed discussion of this assumption is given in Section 6.2. In addition, we also assume constant filling factors, path length, and temperature for the Hα and the X factor for the CO.

To obtain a smoother asymmetric drift correction, following Iorio et al. (2017), we use functional forms to describe the radial velocity dispersion profiles and the elements in the logarithm in Equation (7). The velocity dispersion is fitted by polynomials $\sigma_p(R, n_p)$ with the degree n_p equal to or lower than 3. On the other hand, we fit $\sigma_V^2 \Sigma_{\rm obs}\cos i$ by the function (Bureau & Carignan 2002)

$$f(R) = f_0\left(\frac{R_c}{\rm arcsec} + 1\right)\left(\frac{R_c}{\rm arcsec} + e^{\frac{R}{R_d}}\right)^{-1}, \tag{9}$$

where f_0 is the normalization factor, and R_c and R_d are the characteristic radii. Combining Equations (7) and (9), we get

$$V_A^2 = R\frac{\sigma_p^2(R, n_p)e^{\frac{R}{R_d}}}{R_d}\left(\frac{R_c}{\rm arcsec} + e^{\frac{R}{R_d}}\right)^{-1}. \tag{10}$$

No error of asymmetric drift correction is included in this study. The calculated V_A for each galaxy is shown in Figures C1 and C2. As expected, Hα tends to have higher V_A due to its large velocity dispersion. In general, we did not find any radial trend of V_A statistically.

5.2.2. Discrepancy in the Velocity of CO–Hα after Asymmetric Drift Correction

Figure 5 shows the KDD of ΔV from both ALMaQUEST KSS and EDGE-CALIFA KSS after ADC, which is denoted as

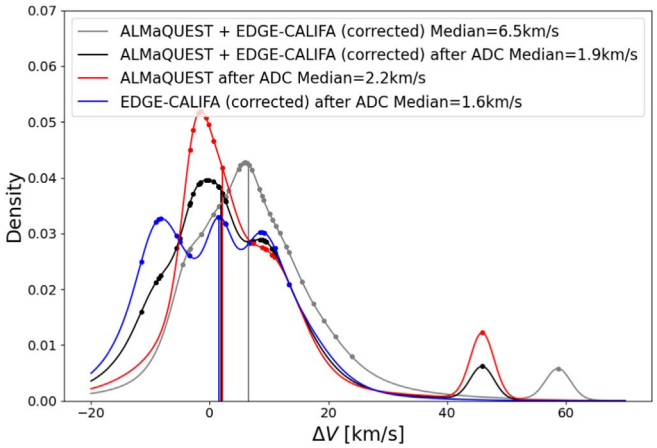

Figure 5. KDD of ΔV after ADC for both the CO and Hα rotation curves. The gray curve is the KDD of ΔV before ADC in ALMaQUEST+EDGE-CALIFA KSS (the gray curve in 3), and the black curve is the KDD of ΔV after ADC in ALMaQUEST+EDGE-CALIFA KSS. The red curve is the KDD of ΔV in the ALMaQUEST sample KSS after ADC. The blue one is the KDD of ΔV in the EDGE-CALIFA sample KSS after ADC.

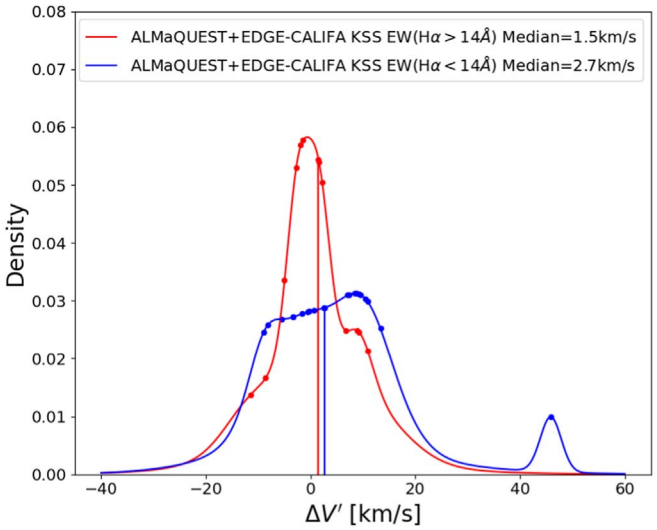

Figure 6. KDD of ΔV after ADC for both CO and Hα rotation curves. The entire samples are separated into two groups based on the criteria EW($H\alpha$) = 14 Å.

$\Delta V'$ hereafter. Compared to Figure 3, we can see that ΔV is reduced in each of the samples after performing the ADC. The median value of $\Delta V'$ becomes 1.9 km s^{-1}, as opposed to the original value of ΔV (= 6.5 km s^{-1}). This result suggests that the source of Hα emission is partially sustained by radial pressure.

5.3. Presence of eDIG

Previous studies in the literature have shown that the rotation speed of eDIG decreases with increasing height above the midplane of the galaxy (Bizyaev et al. 2017; Levy et al. 2019). Such a vertical gradient in the rotational velocity could be responsible for the observed slower Hα rotation (Levy et al. 2018; Espinosa-Ponce et al. 2020; Sánchez 2020). Lacerda et al. (2018) suggest that EW(Hα) is a good proxy for diagnosing the ionization mechanism. Emissions with EW(Hα) >14 Å trace the region where ionization is dominated by the H II region located in the midplane of the galaxies, whereas emissions with EW(Hα) < 3 Å have recently been argued to primarily come from evolved, low-mass stars (i.e., HOLMES) but the origin is still not well established. While the sources of the faint ionized gas have not been well established (e.g., Haffner et al. 2009), the EW(Hα) in between is likely the mixture of these two regions. Following Haffner et al. (2009), we use the flux-weighted average of EW(Hα) in the region where we calculate ΔV in each galaxy to divide our galaxies into two groups based on an EW(Hα) = 14 Å cut. The Hα intensity maps and the EW(α) maps are taken from the MaNGA DR15 PIPE3D value-added products (Sánchez et al. 2016a, 2016b). We simply assume the presence of eDIG is negligible in the high EW(Hα) group, whereas it might be non-negligible in the low EW(Hα) group.

We plot the $\Delta V'$ density distribution for these two groups in Figure 6. Both groups show density distribution centered at the origin, but the high EW(Hα) group has a much smaller dispersion. We note that for the low EW(Hα) group, the ADC might not be accurate because of the following reasons: (i) the presence of eDIG contaminates the Hα velocity dispersion on the midplane; (ii) the assumption we made in Section 5.2 (e.g., thin disk, constant scale height, etc) is no longer valid. Hence, the asymmetric correction alone for these galaxies may not be accurate, which leads to a larger dispersion. Therefore, this result suggests that the eDIG is likely to play a role in the discrepancy in the velocity of CO–Hα, as suggested by Levy et al. (2018).

5.4. MaNGA-CALIFA Systematics

The results of this work assume that the rotation curves based on the MaNGA data are accurate and the MaNGA-CALIFA systematics is attributed to the CALIFA data. Although the exact cause of the MaNGA-CALIFA systematics is not well known, this is a reasonable choice based on the fact that the MaNGA survey has higher spectral resolution, better control of instrumental dispersion, and potentially lower systematics (Bundy et al. 2015; Law et al. 2021). For comparison, we discuss an opposite case, in which the offset is caused by the systematics in the MaNGA data only. We apply the correction of the MaNGA-CALIFA systematics to ALMaQUEST KSS. In this scenario, the median value of ΔV and the $\Delta V'$ in ALMaQUEST+EDGE-CALIFA KSS become greater, 15.0 and 10.8 km s^{-1}, respectively, as shown in Figure 7. This result suggests that while asymmetric drift correction again is able to further reduce ΔV, some other mechanism(s) is needed to fully account for the discrepancy in the velocity of CO–Hα, which is beyond the scope of this work.

6. Discussion

6.1. Robustness of the Rotation Curves and the ADC Corrections

The spectral resolutions of both the MaNGA IFS ($\sigma_{\rm inst} \approx$ 70 km s^{-1}) and the EDGE-CALIFA survey ($\sigma_{\rm inst} \approx 116$ km s^{-1}) of Hα are in general higher than the intrinsic astrophysical dispersion $\sigma_{\rm H\alpha}$. Hence, it is crucial to test if the relatively low spectral resolution of Hα influences the rotation curves and the ADC corrections. Hence, We convolve our ALMaQUEST KSS CO data cubes, which have an original spectral resolution of $\sigma_{\rm inst} \approx 11$ km s^{-1}, to the resolution of the CALIFA Hα observation ($\sigma_{\rm inst} \approx 116$ km s^{-1}) with a Gaussian kernel and use 3DB to fit the CO data cube again. After this process, following the previous procedure, we compare the

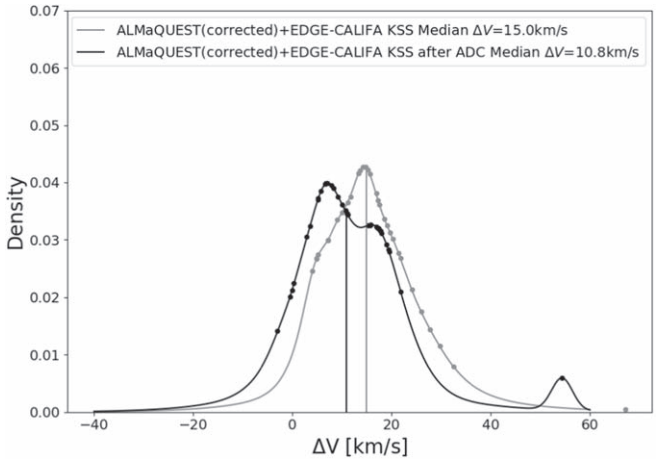

Figure 7. KDD of ΔV and $\Delta V'$ in ALMaQUEST+EDGE-CALIFA KSS under the scenario that the MaNGA-CALIFA systematics is corrected on the ALMaQUEST KSS.

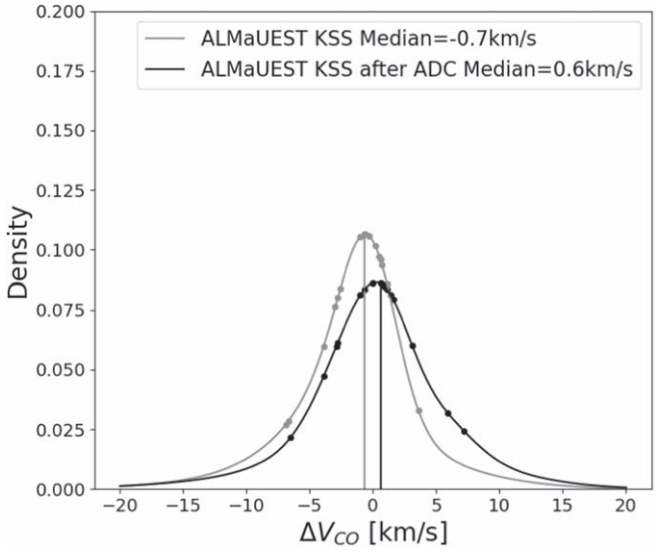

Figure 8. We compare the $V_{\rm rot}$(CO) fit from the original ALMaQUEST KSS data cubes, which have a spectral resolution of $\sim$11 km s^{-1}, to the $V_{\rm rot}$(CO) fit from the convolved ALMaQUEST KSS data cube, which has a spectral resolution of $\sim$116 km s^{-1}. The gray curve shows the KDD of $\Delta V_{\rm CO}$ before the ADC, and the black one is for the one after the ADC ($\Delta V'_{\rm CO}$).

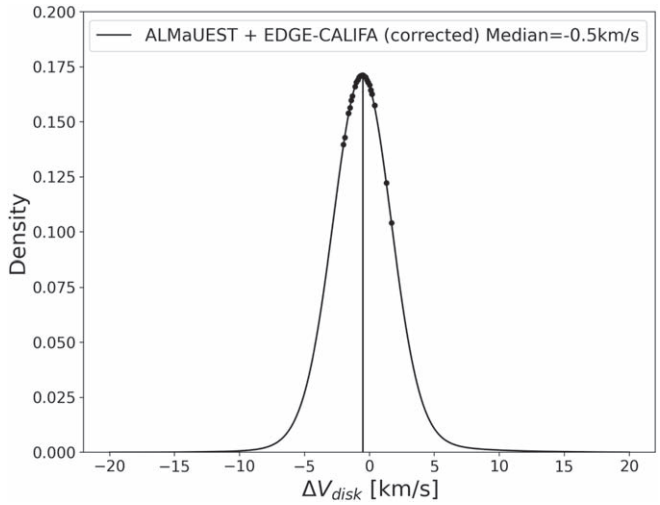

Figure 9. ΔV distribution between $V_{\rm rot}$, $z = 100$ and 1000 pc.

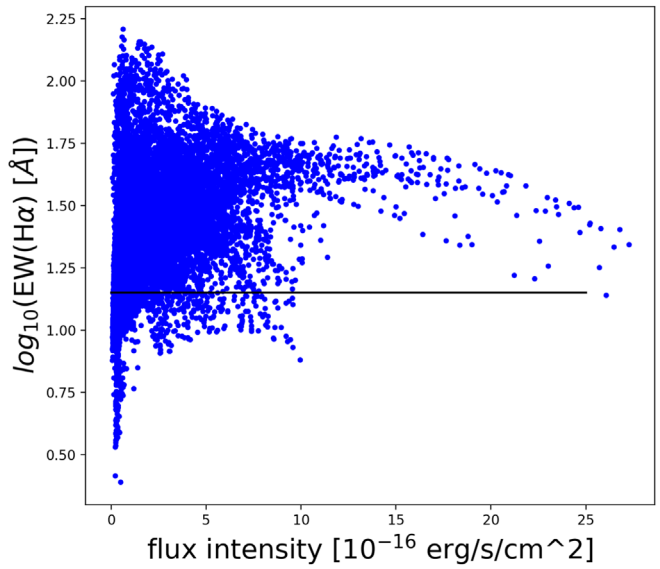

Figure 10. Scatter plots of spaxels that lie in the regions where we calculate ΔV in the high EW group. The black horizontal line denotes EW = 14 Å.

rotation curves derived from the original CO data to the rotation curves derived from the convolved CO data (using the same method described in Section 5.1, denoted as $\Delta V_{\rm CO}$). The comparison of the rotation curves after ADC correction is denoted as $\Delta V'_{\rm CO}$. The result is shown in Figure 8. As can be seen, both the $\Delta V_{\rm CO}$ and $\Delta V'_{\rm CO}$ density distribution show a Gaussian-like distribution centered at zero. By combining this result and the fact that the velocity dispersion of Hα is usually higher than that of CO, we conclude that (i) the systematic discrepancy in the velocity between CO and Hα that we found is not sensitive to their different spectral resolutions within the range considered in this work; (ii) statistically, the ADC applied to the rotation curves presented in this work are reliable.

6.2. Thin Disk Assumption

The discussion in this work so far relies on the thin disk assumption. With the presence of eDIG, the thin disk assumption is no longer valid. Hence, it is crucial to investigate whether the thin disk assumption influences our result or not. The most straightforward test to do is to use 3DB to fit our galaxies again by setting a larger scale height. We refit ALMaQUEST KSS and EDGE-CALIFA KSS again with a scale height of 1 kpc, and then compare the fit result to the ones with a scale height of 100 pc. The comparison is shown in Figure 9. As can be seen, there is little impact on the rotational velocity. The same result is found in the velocity dispersion.

Figure 10 shows scatter plots of spaxels that lie in the region where we calculate ΔV in the large EW(Hα) group. As can be seen, most of the spaxels (90%) in these regions have EW(Hα) larger than 14 Å, which are usually H II regions. Hence, the presence of eDIG has little impact on the 3DB fit results for the high EW group galaxies. Therefore, we conclude that the thin disk model and a constant scale height are reasonable for these galaxies and the main conclusion of this work still holds.

6.3. Dynamical Mass Measurement

From the result presented above, one can find that the mass model based on ionized gas could potentially be biased low. For a galaxy with an intrinsic circular velocity of 200 km s^{-1} (the median value in our sample), $\Delta V = 6.5$ km s^{-1} (the median value of ΔV in our sample) would underestimate the total dynamical mass by ∼6%. In this study, we find that by applying ADC, the discrepancy between the Hα and CO rotation curve can be further reduced to 1.9 km s^{-1}, corresponding to a 2% underestimation in the dynamical mass measurement based on the Hα rotation curve. In the future, we will compare the dynamical mass derived from the Hα rotation curves in our galaxies with other studies, such as those of Zhu et al. (2018) and Aquino-Ortíz et al. (2020).

7. Conclusion

By combining the ALMaQUEST and the EDGE-CALIFA surveys, we analyze and compare the CO and Hα rotation curves in 34 rotation-dominated galaxies. Before combining the two data sets, we first compare the Hα rotation curves in eight MaNGA-CALIFA overlapping galaxies. We find systematics between the Hα rotation curves measured from the MaNGA data and that from the CALIFA data, where the CALIFA rotation curves tend to have slower rotational velocities by 8.5 km s^{-1}. We compensate the systematics by adding 8.5 km s^{-1} to the CALIFA data set, and the conclusion is based on this premise. Our principal conclusions are:

1. 56% of our galaxies show smaller Hα rotational velocity (10/17 in ALMaQUEST KSS, and 9/17 in EDGE-CALIFA KSS). The median value of the difference in the rotational velocity of CO–Hα is 6.5 km s^{-1} (5.7 km s^{-1} for the ALMaQUEST samples, and 6.7 km s^{-1} for the EDGE-CALIFA samples). The remaining 44% of the sample shows consistency between CO and Hα rotations. For a galaxy with a circular velocity of 200 km s^{-1} (the median value in our sample), $\Delta V = 6.5$ km s^{-1} would lead to an ∼6% underestimation in the dynamical mass.
2. The magnitude of the differences between the CO and Hα rotational velocity, ΔV, correlates with the difference between CO and Hα velocity dispersion, which suggests that the gas radial pressure gradient plays a key role in explaining the discrepancy in the velocity of CO–Hα. Under the assumption that the turbulence pressure dominates the radial pressure on the Hα emitting gas, we apply ADC to both the CO and Hα rotation curves. After ADC, the median value of the difference in the CO–Hα rotational velocity reduces to 1.9 km s^{-1} (2.2 km s^{-1} for ALMaQUEST KSS, and 1.6 km s^{-1} for EDGE-CALIFA KSS), which corresponds to an ∼2% underestimation of dynamical mass based on the Hα measurement in the case of the circular velocity being 200 km s^{-1}.
3. We divided our sample into two groups based on the EW(Hα) = 14 Å cut. The ionization in the high EW group is dominated by the H II regions. For the low EW group, the contribution of eDIG to the Hα emission is non-negligible. The median value of ΔV after ADC is 1.5 km s^{-1} in the high EW group, which is 2.7 km s^{-1} in the low EW group. Both groups show the density distribution centered at the origin, but the low EW(Hα) group has a much larger dispersion, which could be due to the presence of eDIG.

Our result suggests both radial pressure gradient and the presence of eDIG are responsible for the difference in the velocity between CO and Hα rotations. This result suggests that it is possible to recover the circular velocity from the Hα rotation curves if properly taking these two factors into account.

We thank the anonymous referee for providing helpful comments, which greatly improved the quality of this work. This work is supported by the Academia Sinica under the Career Development Award CDA107-M03 and the Ministry of Science & Technology of Taiwan under the grant MOST 108-2628-M-001-001-MY3. H.A.P. acknowledges support by the Ministry of Science and Technology of Taiwan under grant 110-2112-M-032-020-MY3. The authors would like to thank the staffs of the East Asia and North America ALMA ARCs for their support and continuous efforts in helping produce high-quality data products. This paper makes use of the following ALMA data: ADS/JAO.ALMA#2015.1.01225.S, ADS/JAO.ALMA#2017.1.01093.S, ADS/JAO.ALMA#2018.1.00541.S, and ADS/JAO.ALMA#2018.1.00558.S. ALMA is a partnership of ESO (representing its member states), NSF (USA) and NINS (Japan), together with NRC (Canada), MOST and ASIAA (Taiwan), and KASI (Republic of Korea), in cooperation with the Republic of Chile. The Joint ALMA Observatory is operated by ESO, AUI/NRAO, and NAOJ.

Appendix A
SFR Surface Density

To calculate $\Sigma_{\rm SFR}$ within the region where we determine ΔV, for each galaxy, we first pick the spaxel in which S/N > 3 in the emission lines Hα, Hβ, [O III]λ5007, and [S II]$\lambda\lambda$6717, 31. To take into account the effect of dust extinction on SFR, we use the Balmer decrement to correct the Hα flux based on an equation that assumes a Cardelli et al. (1989) extinction curve

$$A_{\rm H_\alpha} = 5.86 \log\left(\frac{F_{\rm H_\alpha}}{2.86 F_{\rm H_\beta}}\right), \quad \text{(A1)}$$

where $F_{\rm H_\alpha}$ and $F_{\rm H_\beta}$ are the fluxes of the Hα and Hβ emission lines, respectively. Then, we calculate the SFR spaxel by spaxel based on the the equation (Rosa-González et al. 2002)

$$\mathrm{SFR} = 7.9 \times 10^{-42} F_{\rm H_\alpha} 10^{\frac{A_{\rm H_\alpha}}{2.5}}, \quad \text{(A2)}$$

which assumes a Salpeter initial mass function. When calculating $\Sigma_{\rm SFR}$, only the star-forming spaxels classified with the [S II] BPT diagnostic (Kewley et al. 2001, 2006) are included. Finally, we sum the SFR spaxels within the region where we determined ΔV and divided it by the deprojected area the inclination correction applied.

Appendix B
Test on the MaNGA-CALIFA Overlapping Galaxies

This section aims at investigating the systematic between the MaNGA and the CALIFA Hα data. We match the MaNGA and the CALIFA galaxies (Sánchez et al. 2016a, 2016b), and 37 overlapping galaxies are found. To make the result applicable to the galaxies in our study, we apply the same selection criteria described in Section 4.2, and finally, eight galaxies are included in this test.

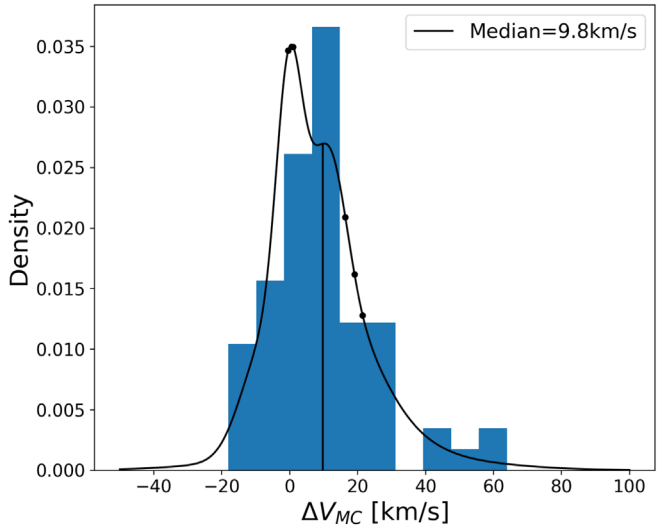

Figure B1. $\Delta V_{\rm MC}$ distribution. The blue bins are histograms of the difference in the velocity of the radial bins in all galaxies. This result shows that the CALIFA fit result tends to have a slower rotational velocity by 9.8 km s^{-1}.

We use 3DB to fit the Hα rotation curves for these overlapping galaxies using both the MaNGA and CALIFA data cubes. We follow the strategy described in Section 4. For each galaxy, we use the same inclination and position for the MaNGA and CALIFA fittings. The inclinations and the position angles are based on the MaNGA best fit.

B.1. Comparison of the Rotation Curves

After comparing the MaNGA and the CALIFA fitting result in these overlapping galaxies, we found a systematic in the rotational velocity. The best fit of the CALIFA data tends to have a slower rotational velocity by 9.8 km s^{-1}, as shown in Figure B1. We adopt the definition of ΔV and use it to quantify the difference between the MaNGA and the CALIFA rotation curve fit results in these overlapping galaxies, denoted as $\Delta V_{\rm MC}$. To test the robustness of $\Delta V_{\rm MC}$, we use a bootstrap method to resample the differences in the velocity of the radial bins in all galaxies a number of times and calculate the median value of $\Delta V_{\rm MC}$. Finally, the systematics of 8.5 km s^{-1} with a dispersion of 1.3 km s^{-1} is found in the median value of $\Delta V_{\rm MC}$. This result suggests there is systematics between the MaNGA fit result and the CALIFA fit result based on our method. Given that the MaNGA data has a better spectral resolution, we correct ΔVs (i.e., the variance weighted mean of the differences in the velocity $V_{\rm rot,CO}-V_{\rm rot,H\alpha}$, as defined in Section 5.1) in the EDGE-CALIFA KSS value by subtracting 8.5 km s^{-1}.

B.2. Comparison of the Radial Velocity Dispersion Profiles

The robustness of the radial velocity dispersion profiles is crucial for calculating a reliable ADC. Compared to H$_\alpha$, the measurement of the CO velocity dispersion should be more robust due to its higher spectral resolution. On the other hand, Law et al. (2021) found that the line spread function (LSF) of the MaNGA Hα lines can be described well by a Gaussian, and the reliability of the astrophysical velocity dispersion of

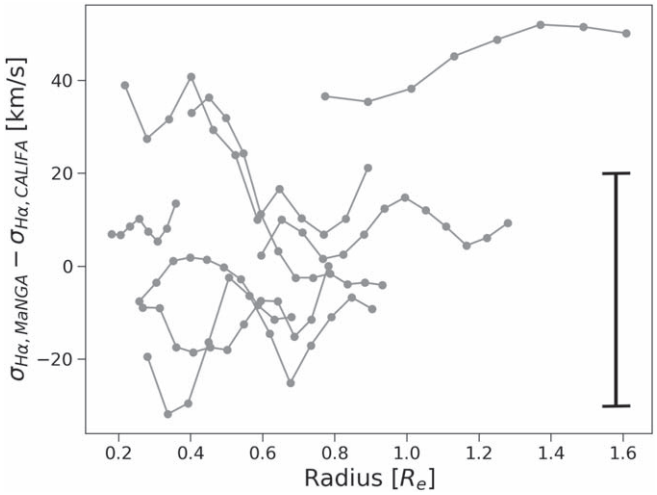

Figure B2. The vertical axis represents the difference in the velocity dispersion between the MaNGA and CALIFA data for the eight MaNGA-CALIFA overlapping galaxies. The horizontal axis is the radius in effective radius. Each gray line presents one galaxy, and the vertical black line presents the typical uncertainty.

20 km s^{-1} could be achieved when the S/N is sufficiently high enough. The low spectral resolution of the CALIFA data, however, raises concern about the reliability of the Hα velocity dispersion measurement in the EDGE-CALIFA KSS. Under the condition that the spectral resolution is much lower than the astrophysical velocity dispersion, the LSF must be well known to get a reliable velocity dispersion. In this study, we adopt the instrumental dispersion of all CALIFA Hα data to be 116 km s^{-1} (Sánchez et al. 2016c). To validate this choice, we compare the Hα radial velocity dispersion profiles in the eight overlapping galaxies measured between the MaNGA data and the CALIFA data.

In Figure B2, the gray lines represent the radial profile of the difference in the velocity dispersion between the MaNGA measurement and the CALIFA measurement for the eight overlapping galaxies. The black vertical line is the typical uncertainty. As one can see, there is no apparent systematics in the velocity dispersion between these two measurements, suggesting that the typical instrumental dispersion we use for the CALIFA galaxies should be representative. On the other hand, the scatter of the velocity dispersion offset simply means the ADC measurement is subject to the uncertainty in the individual velocity dispersion measurement, which is not considered in this study.

Appendix C
Other Plots

Figure C1 shows the velocity maps, rotation curves and the radial velocity dispersion profiles in the ALMaQUEST KSS. The same as Figure C1 but for the EDGE-CALIFA KSS galaxies is shown in Figure C2. Figure C3 shows the relation between the ΔV and several parameters.

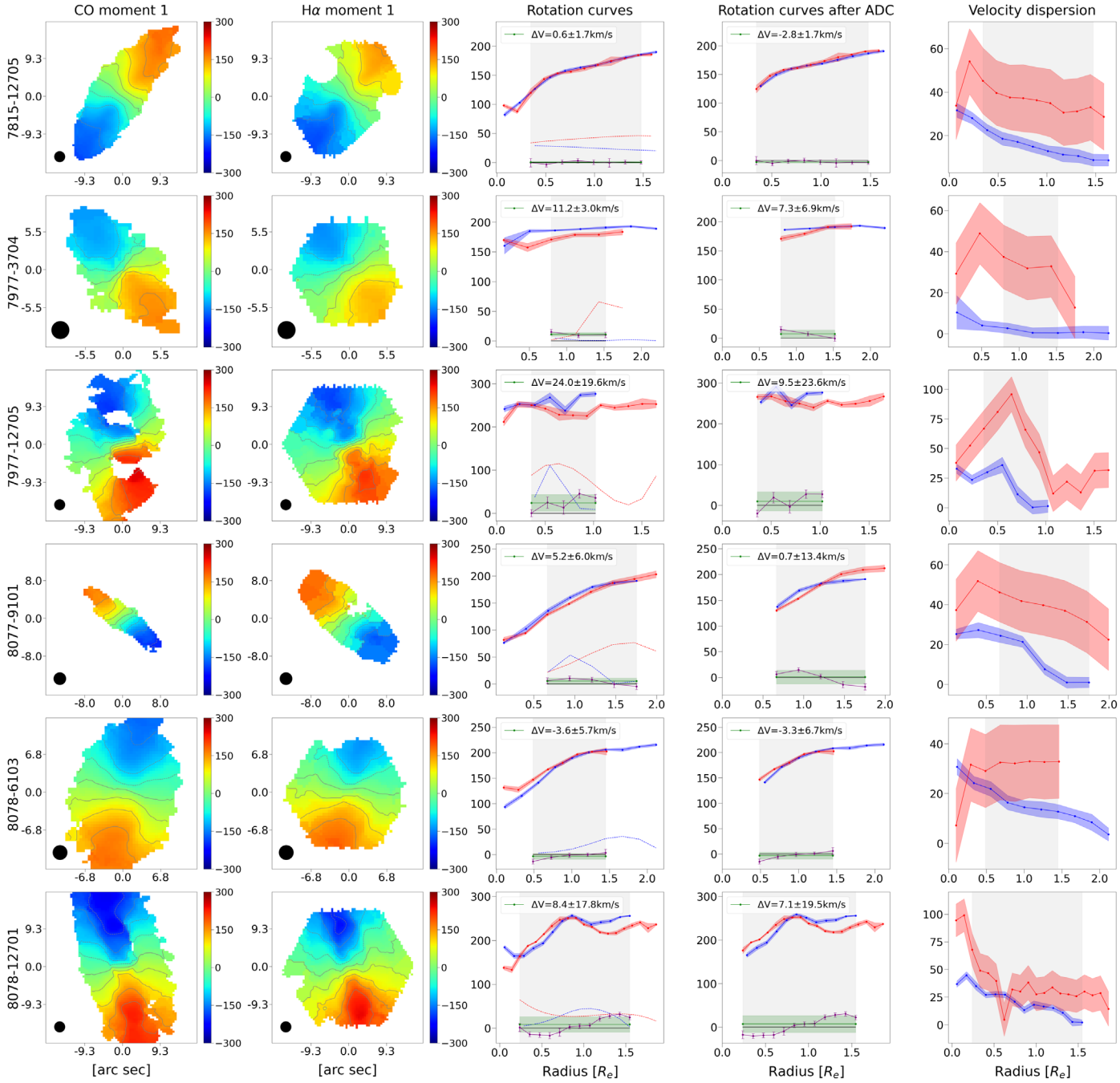

Figure C1. The first column shows CO velocity maps for ALMaQUEST KSS. The color in these maps varies between ± 300 km s^{-1} with negative velocity in blue. The interval of the contours is 50 km s^{-1}. Both axis values show the offset in arcsec from the center of the image. The black circles at the bottom left are the typical resolution of the ALMaQUEST KSS data, which is $2\farcs5$. The second column shows the Hα velocity maps for ALMaQUEST KSS with features identical to those in the first column. The third column shows the CO and Hα rotation curves. The x-axis is the galactocentric radius in the unit of effective radius (R_e), and the y-axis is the velocity in kilometers per second. The blue ones represent CO rotation curves and the red ones represent Hα rotation curves. The purple lines connect the differences in the velocity between $V_{\rm rot}$(CO) and $V_{\rm rot}$(Hα) at each radial bin. ΔV, which is the variance weighted mean of the differences in the velocity, is calculated within the gray area. The error in ΔV is the standard deviation of the differences in the velocity in the sample points. The green line shows the value of ΔV. The shadow areas present the errors of each quantity. The blue and red dashed lines represent the V_A radial profiles of CO and Hα, respectively. The fourth column shows the CO and Hα rotation curves after ADC. The features in the fourth column are identical to those in the third column. The fifth column shows the CO and Hα radial velocity dispersion profile. The x-axis is the galactocentric radius in the unit of R_e and the y-axis is the velocity dispersion in kilometers per second. The CO rotation curves are shown in blue and the Hα rotation curves are shown in red.

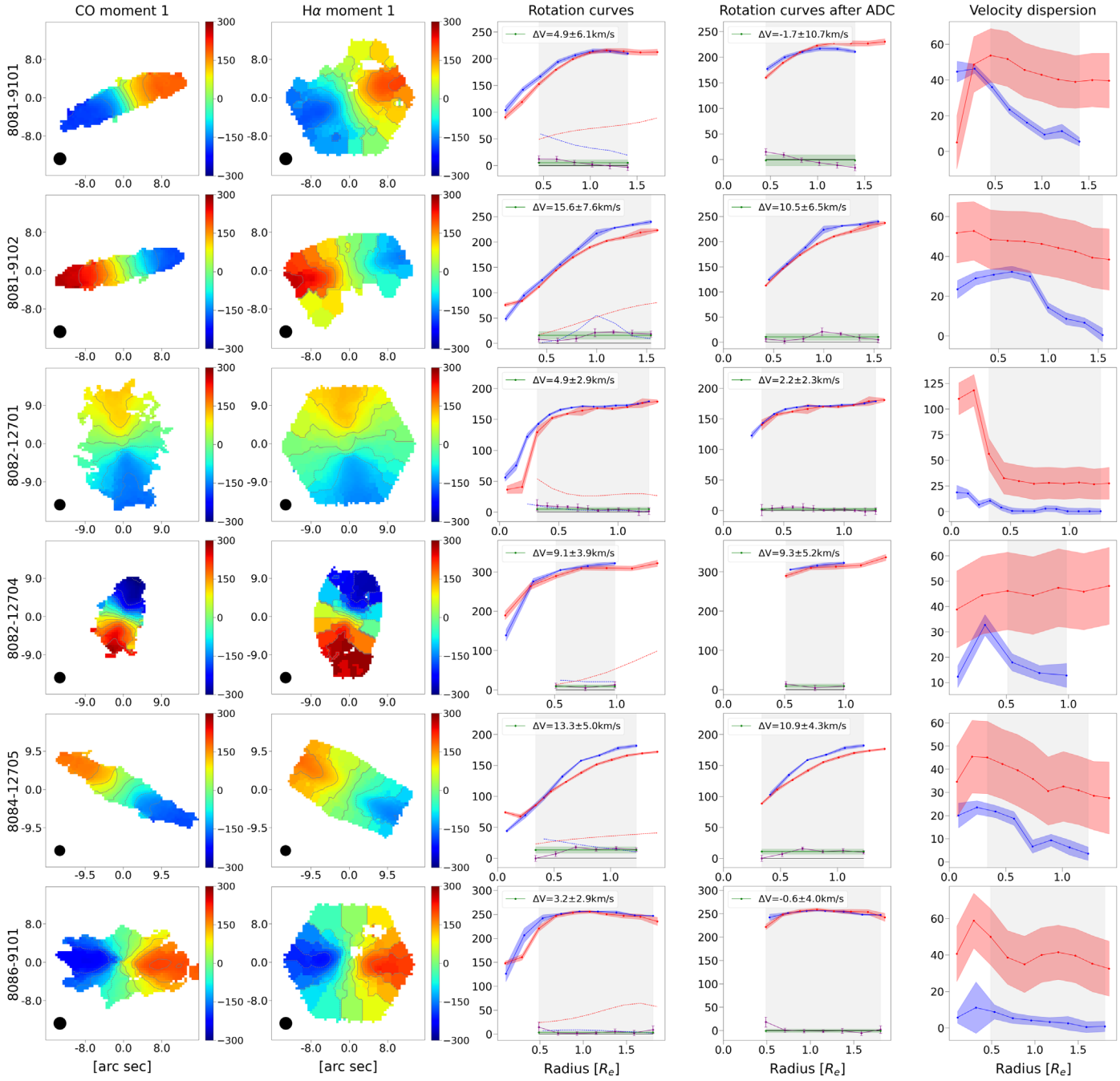

Figure C1. (Continued.)

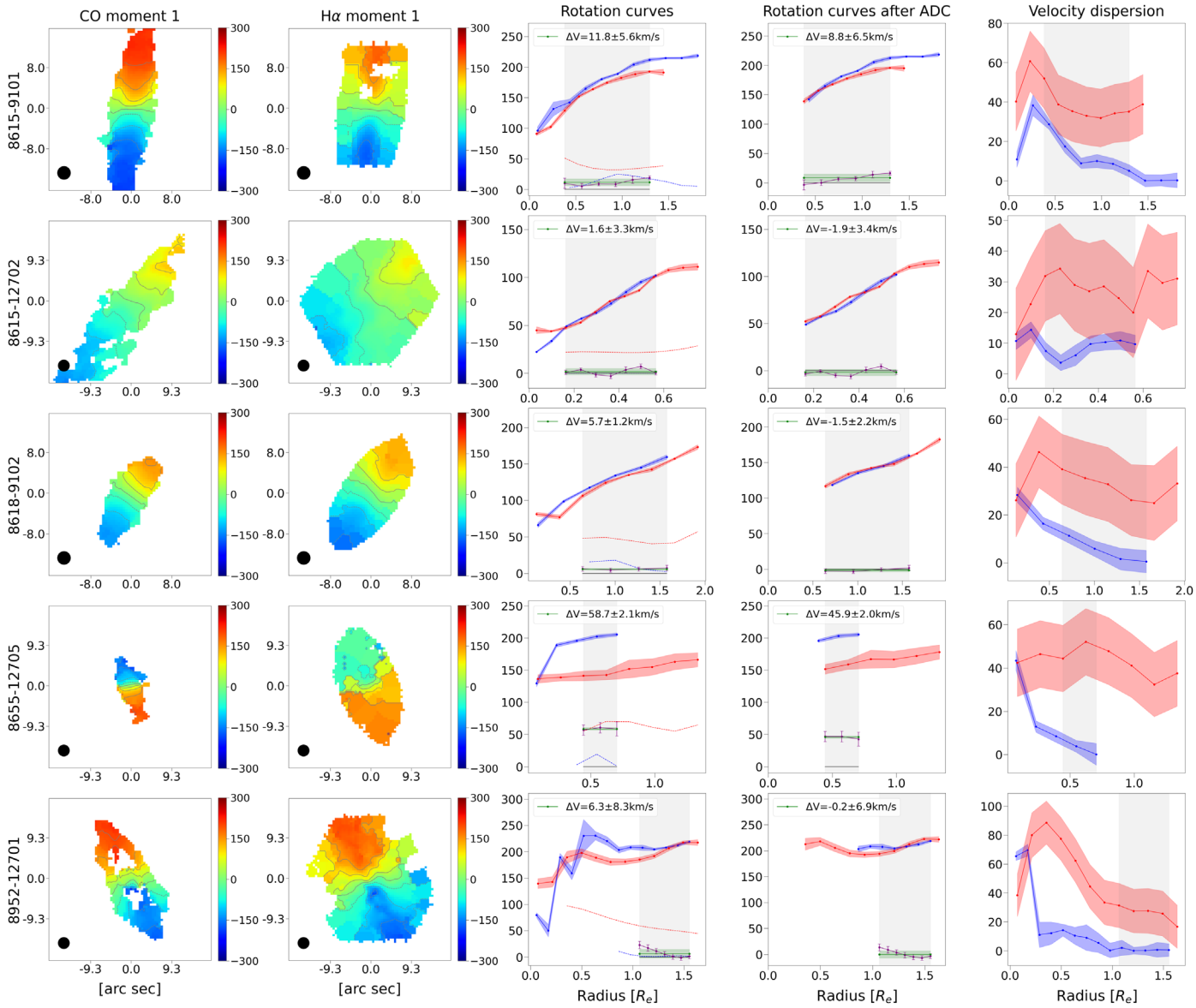

Figure C1. (Continued.)

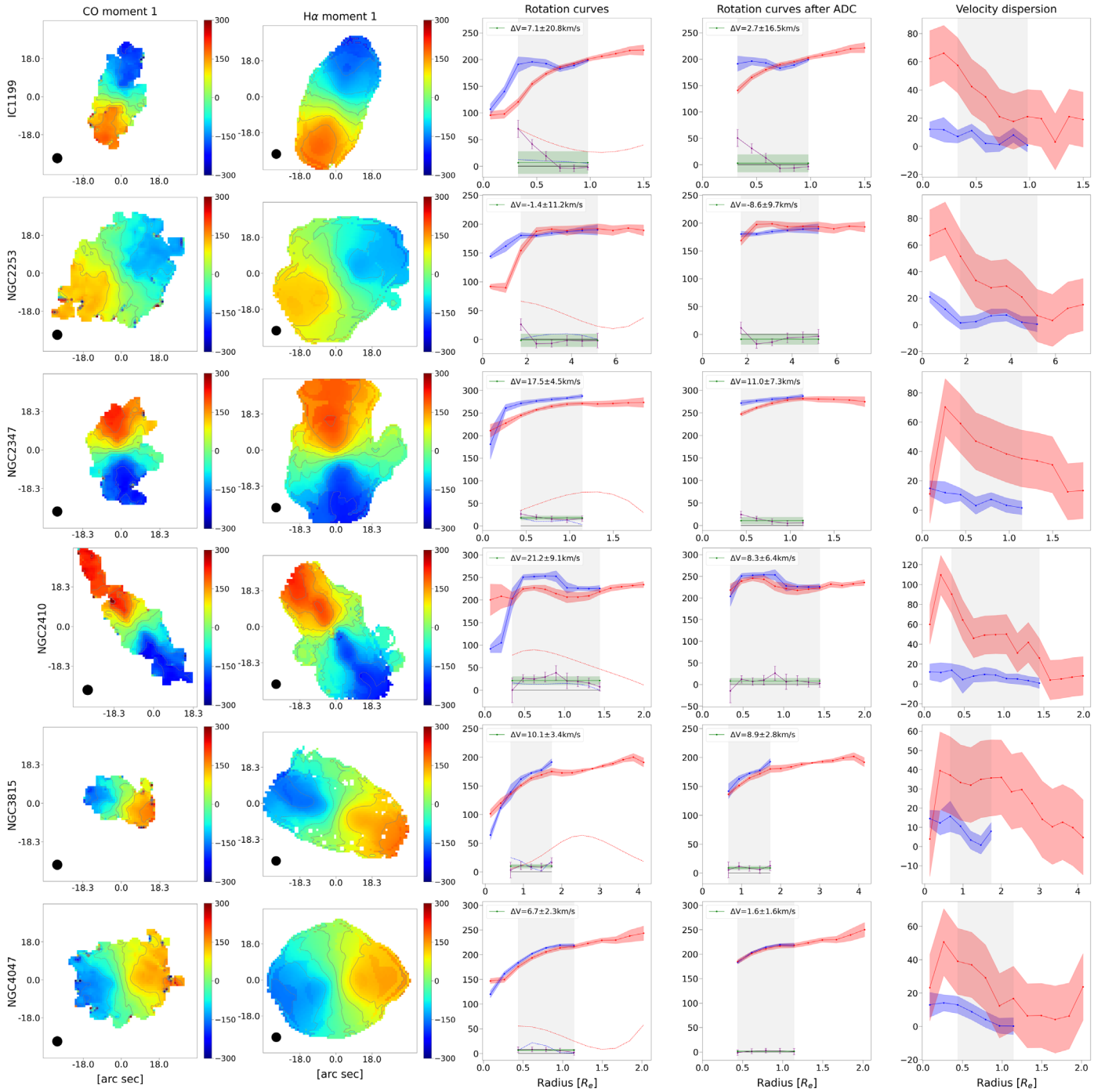

Figure C2. The same as Figure C1 but for the EDGE-CALIFA KSS galaxies. The black circles at the bottom left in the first two columns are the typical resolution of EDGE-CALIFA KSS data, which is $4\farcs5$. We note that the Hα rotation curves (and hence ΔV) in the third and the fourth columns have been corrected for the MaNGA-CALIFA systematics.

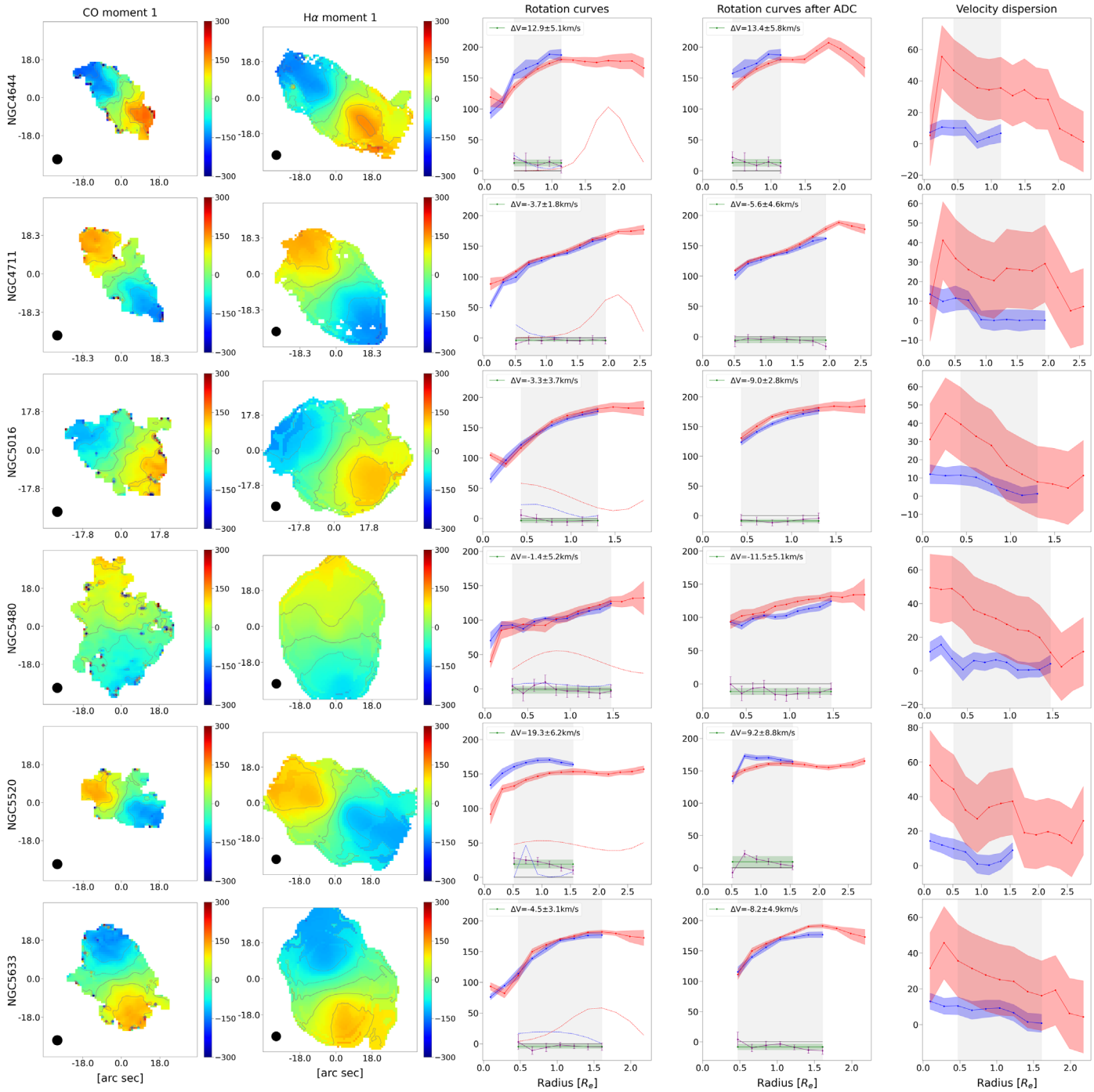

Figure C2. (Continued.)

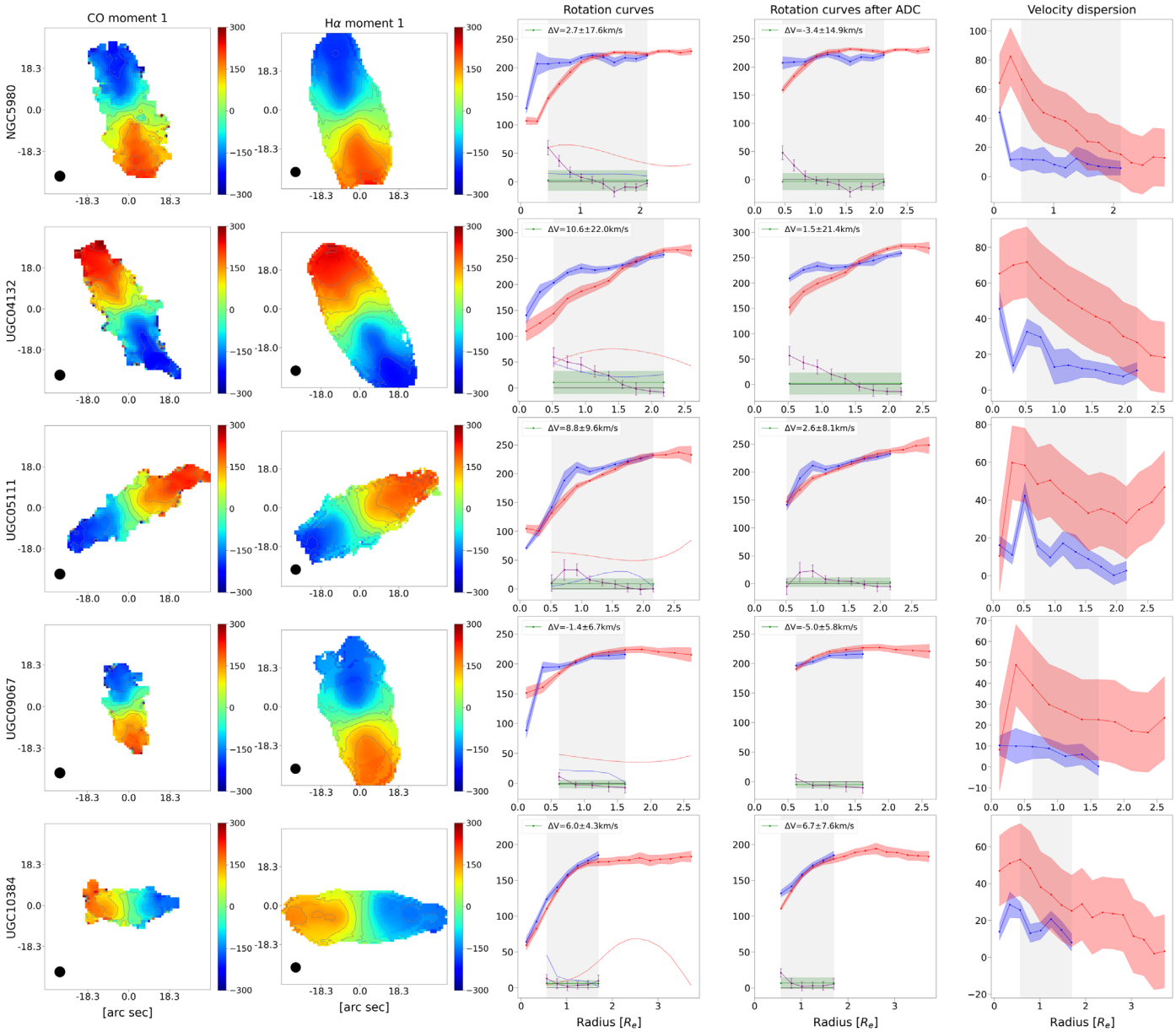

Figure C2. (Continued.)

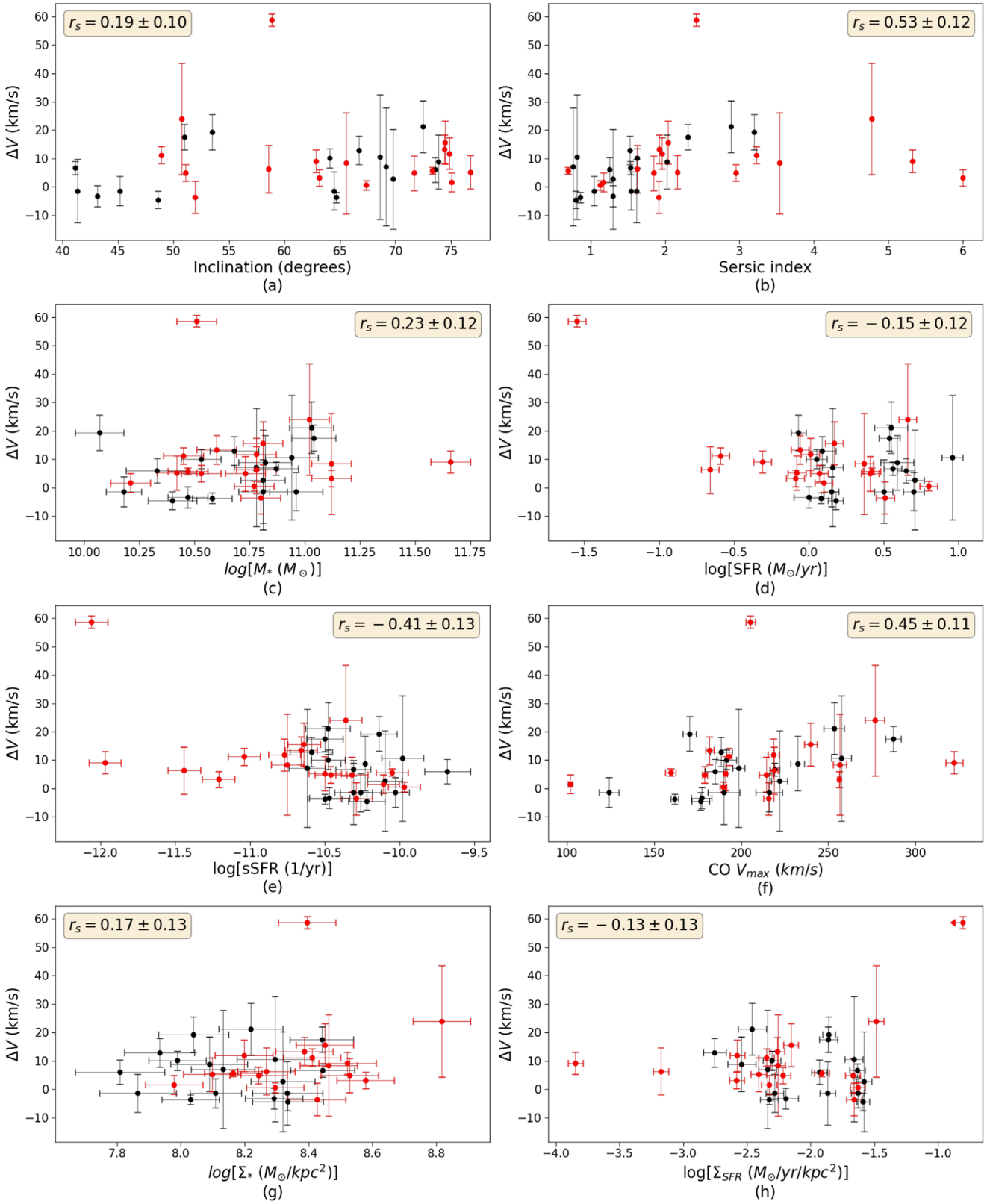

Figure C3. No apparent trend is found between ΔV and (a) inclination, (b) Sérsic index, (c) stellar mass, (d) SFR, (e) sSFR, (f) CO $V_{\rm max}$, (e) Σ_* and (h)$\Sigma_{\rm SFR}$. The red points represent ALMaQUEST KSS, and the black points represent EDGE-CALIFA KSS. The Sérsic index comes from the SDSS NSA catalog. For the ALMaQUEST KSS galaxies, the stellar mass and SFR are listed in Lin et al. (2020). For the EDGE-CALIFA KSS galaxies, the stellar mass and SFR are from Bolatto et al. (2017). Σ_* and $\Sigma_{\rm SFR}$ in this figure are calculated within the region where ΔV is calculated. See Appendix A for more details.

ORCID iDs

Yung-Chau Su https://orcid.org/0000-0001-6106-5383
Lihwai Lin https://orcid.org/0000-0001-7218-7407
Hsi-An Pan https://orcid.org/0000-0002-1370-6964
Carlos López Cobá https://orcid.org/0000-0003-1045-0702
Bau-Ching Hsieh https://orcid.org/0000-0001-5615-4904
Sebastián F. Sánchez https://orcid.org/0000-0001-6444-9307
Mallory D. Thorp https://orcid.org/0000-0003-0080-8547
Martin Bureau https://orcid.org/0000-0003-4980-1012
Sara L. Ellison https://orcid.org/0000-0002-1768-1899

References

Aquino-Ortíz, E., Sánchez, S. F., Valenzuela, O., et al. 2020, ApJ, 900, 109
Begeman, K. G. 1989, A&A, 223, 47
Bizyaev, D., Walterbos, R. A. M., Yoachim, P., et al. 2017, ApJ, 839, 87
Blanton, M. R., Kazin, E., Muna, D., Weaver, B. A., & Price-Whelan, A. 2011, AJ, 142, 31
Bolatto, A. D., Wong, T., Utomo, D., et al. 2017, ApJ, 846, 159
Broeils, A. H., & Courteau, S. 1997, in ASP Conf. Ser. 117, Dark and Visible Matter in Galaxies and Cosmological Implications, ed. M. Persic & P. Salucci (San Francisco, CA: ASP), 74
Bundy, K., Bershady, M. A., Law, D. R., et al. 2015, ApJ, 798, 7
Bureau, M., & Carignan, C. 2002, AJ, 123, 1316
Cardelli, J. A., Clayton, G. C., & Mathis, J. S. 1989, ApJ, 345, 245
Dalcanton, J. J., & Stilp, A. M. 2010, ApJ, 721, 547
Davis, T. A., Alatalo, K., Bureau, M., et al. 2013, MNRAS, 429, 534
de Blok, W. J. G., McGaugh, S. S., & Rubin, V. C. 2001, AJ, 122, 2396
de Blok, W. J. G., Walter, F., Brinks, E., et al. 2008, AJ, 136, 2648
Di Teodoro, E. M., & Fraternali, F. 2015, MNRAS, 451, 3021
Douglass, K. A., Smith, J. A., & Demina, R. 2019, ApJ, 886, 153
Epinat, B., Contini, T., Le Fèvre, O., et al. 2009, A&A, 504, 789
Espinosa-Ponce, C., Sánchez, S. F., Morisset, C., et al. 2020, MNRAS, 494, 1622
Haffner, L. M., Dettmar, R. J., Beckman, J. E., et al. 2009, RvMP, 81, 969
Iorio, G., Fraternali, F., Nipoti, C., et al. 2017, MNRAS, 466, 4159
Kelz, A., Verheijen, M. A. W., Roth, M. M., et al. 2006, PASP, 118, 129
Kewley, L. J., Dopita, M. A., Sutherland, R. S., Heisler, C. A., & Trevena, J. 2001, ApJ, 556, 121
Kewley, L. J., Groves, B., Kauffmann, G., & Heckman, T. 2006, MNRAS, 372, 961
Kuzio de Naray, R., McGaugh, S. S., & de Blok, W. J. G. 2008, ApJ, 676, 920
Lacerda, E. A. D., Cid Fernandes, R., Couto, G. S., et al. 2018, MNRAS, 474, 3727
Lang, P., Meidt, S. E., Rosolowsky, E., et al. 2020, ApJ, 897, 122
Law, D. R., Cherinka, B., Yan, R., et al. 2016, AJ, 152, 83
Law, D. R., Westfall, K. B., Bershady, M. A., et al. 2021, AJ, 161, 52
Leung, G. Y. C., Leaman, R., van de Ven, G., et al. 2018, MNRAS, 477, 254
Levy, R. C., Bolatto, A. D., Sánchez, S. F., et al. 2019, ApJ, 882, 84
Levy, R. C., Bolatto, A. D., Teuben, P., et al. 2018, ApJ, 860, 92
Lin, L., Ellison, S. L., Pan, H.-A., et al. 2020, ApJ, 903, 145
Östlin, G., Amram, P., Masegosa, J., Bergvall, N., & Boulesteix, J. 1999, A&AS, 137, 419
Rogstad, D. H., Lockhart, I. A., & Wright, M. C. H. 1974, ApJ, 193, 309
Rosa-González, D., Terlevich, E., & Terlevich, R. 2002, MNRAS, 332, 283
Sánchez, S. F. 2020, ARA&A, 58, 99
Sánchez, S. F., Avila-Reese, V., Hernandez-Toledo, H., et al. 2018, RMxAA, 54, 217
Sánchez, S. F., García-Benito, R., Zibetti, S., et al. 2016c, A&A, 594, A36
Sánchez, S. F., Kennicutt, R. C., Gil de Paz, A., et al. 2012, A&A, 538, A8
Sánchez, S. F., Pérez, E., Sánchez-Blázquez, P., et al. 2016a, RMxAA, 52, 21
Sánchez, S. F., Pérez, E., Sánchez-Blázquez, P., et al. 2016b, RMxAA, 52, 171
Simon, J. D., Bolatto, A. D., Leroy, A., Blitz, L., & Gates, E. L. 2005, ApJ, 621, 757
Sofue, Y., & Rubin, V. 2001, ARA&A, 39, 137
Swaters, R. A., Sancisi, R., van Albada, T. S., & van der Hulst, J. M. 2009, A&A, 493, 871
van Albada, T. S., Bahcall, J. N., Begeman, K., & Sancisi, R. 1985, ApJ, 295, 305
van den Bosch, F. C., Robertson, B. E., Dalcanton, J. J., & de Blok, W. J. G. 2000, AJ, 119, 1579
Walcher, C. J., Wisotzki, L., Bekeraité, S., et al. 2014, A&A, 569, A1
Westfall, K. B., Cappellari, M., Bershady, M. A., et al. 2019, AJ, 158, 231
Zhu, L., van de Ven, G., van den Bosch, R., et al. 2018, NatAs, 2, 233